Sofia Patomäki

June 2017

Master's Thesis

Theoretical Physics

Characterizing superconducting qubits

Instructors Prof. Mikko Möttönen
Prof. Kari Rummukainen

Supervisors Prof.Mikko Möttönen
Dr. Tech. Joonas Govenius

University of Helsinki
PL 64 (Gustav Hällströmin katu 2)
00014 Helsinki

HELSINGIN YLIOPISTO — HELSINGFORS UNIVERSITET — UNIVERSITY OF HELSINKI

Tiedekunta/Osasto — Fakultet/Sektion — Faculty	Laitos — Institution — Department
Faculty of Science	Department of Physics

Tekijä — Författare — Author
Sofia Patomäki

Työn nimi — Arbetets titel — Title

Characterizing superconducting qubits

Oppiaine — Läroämne — Subject
Theoretical Physics

Työn laji — Arbetets art — Level	Aika — Datum — Month and year	Sivumäärä — Sidoantal — Number of pages
Master's Thesis	June 2017	76

Tiivistelmä — Referat — Abstract

In a quantum computer, the information carriers, which are bits in ordinary computers, are implemented as devices that exhibit coherent superpositions of physical states and entanglement. Such components, known as quantum bits or *qubits*, can be realized with various different types of two-state quantum systems. Quantum computers will be built for computational speed, with hoped for applications especially in cryptography and in other tasks where classical computers remain inefficient.

Circuit quantum electrodynamics (cQED) is a quantum-computer architecture which employs superconducting electronic components and microwave photon fields as building blocks. Compared to cavity quantum electrodynamics (CQED), where atoms are trapped in physical cavities, cQED is more attractive in that its qubits are tunable and conveniently integrable with the electronics already in use. This architecture has shown some of the most promising qubit designs, despite their coherence times reaching tens of microseconds, are still below the state of the art with spin qubits, which reach milliseconds. Coherence times are historically the most relevant parameters describing the fitness of a qubit, although these days not necessarily the limiting factor.

This thesis presents a comprehensive set of theoretical and experimental methods for measuring the characteristic parameters of superconducting qubits. We especially study transmission-line-shunted plasma oscillation qubits, or transmons, and presents experimental results for a single sample. Transmon capacitively couples a superconducting quantum interference device (SQUID) with a coplanar waveguide (CPW) resonator, often with added frequency tunability utilizing an external magnet. The number of superconducting charge carriers tunnelled through a junction in the SQUID are used as qubit degrees of freedom. Readout of the qubit state is carried out by measuring transmission through the CPW. A cryogenic setup is employed with measurement and driving pulses delivered from microwave sources. Steady-state spectroscopy is employed to determine the resonance frequencies of the qubit and the resonator, qubit-resonator coupling constants, and the energy parameters of the qubit. Pulse-modulated measurements are employed to determine the coherence times of the qubit. The related analysis- and simulation programs and scripts are collected to github.com/patomaki.

Avainsanat — Nyckelord — Keywords
Quantum computing, superconducting qubit, transmon, homodyne detection, spectroscopy

Säilytyspaikka — Förvaringsställe — Where deposited

Muita tietoja — Övriga uppgifter — Additional information

Preface

The setup was built and the experiments were carried out in Quantum Computing and Devices group in the Department of Applied Physics of Aalto University. The measured transmon sample was designed by M. Sc. Theo Walter from Quantum Device Lab, ETH Zurich and fabricated in ETH Zurich. I thank Walter, the group leader, Prof. Andreas Wallraff, and the rest of the group for collaboration. I sincerely thank my group leader, Prof. Mikko Möttönen, for giving me the opportunity to expand my understanding in the realms of experimental physics. I am deeply grateful to Dr. Tech. Joonas Govenius for guidance with the setup, as well as insight and conversations in most versatile topics. An equally important member in the group has been M.Sc. Matti Partanen, whom I warmly thank for his great deal of patience, guidance, and sense of humor. I thank M.Sc. Mikael Mieskolainen for reminding me of the importance of statistics. I also wish to send my thanks to M.Sc. Uri Vool, for a nice discussion on circuit quantization.

For good company I thank my fellow students and friends from University of Helsinki, Aalto university and elsewhere. Without Joona, Joonas, Otto, Roope, and many other students, studying would probably have been a less enjoyable adventure. I want to thank Mikael for all the physics discussions, and for keeping up my spirit. Close ones make make life worthwile. Finally, I wish to send thanks to all of my family for their love and support, especially to my mother for encouraging me to work hard and to my late father for having fuelled my spark of curiosity.

List of symbols and notation

Bolded symbols represent vectors. Unless the symbol is found from the list below, capital letters are used to denote possibly non-commuting objects under multiplication. Hat on top of a symbol implies a quantum operator.

$\|\Sigma\rangle$	Quantum state vector labeled by quantum numbers Σ,
$\mathbf{A}$	Vector potential of electrodynamics
A_0	Scalar potantial of electrodynamics
$\hat{a}$	Lowering operator that annihilated one quantum from a quantum state
$\hat{a}^\dagger$	Raising operator, that creates one excitation quantum to a quantum state
abs	Absolute value
C_i	Capacitance of a component i
cost	Cost function, minimized in fitting problems
div	Integer quotient in division
e	Unit charge, approximately 1.602×10^{-19} C
E_C	Electrostatic energy of a Josephson junction capacitor, charged with one Cooper pair
E_J	Josephson energy of a Josephson junction
E_n	The nth energy level of a system
f	Frequency
$g_{i,j}$	Coupling constant between subsystems i and j
G	Conductance of a normal conductor
h	Planck constant, approximately 6.626×10^{-34} Js
$\hbar$	Reduced Planck constant, $h/(2\pi)$
H	Hamiltonian function of a classical system
$\hat{H}$	Hamiltonian operator of a quantum system
I	Electric current
I_c	Critical current through a Josephson junction
im	Imaginary part
int	A function that rounds a real number to the closest integer
$\mathbf{j}$	Current density
k_B	Boltzmann constant, approximately 1.380×10^{-23} J/K
k_n	An integer-valued function related to solution of energy levels of CPB

L	Lagrange function of a classical system
L_i	Inductance of a component i
ma	Mathieu's characteristic a; a special function
mod	Modulo operation
$\hat{n}$	Number operator for the number of excitations in a harmonic oscillator
$\mathbf{n}$	Unit vector that parametrizes a direction
P	Power
$\mathcal{P}$	Probability
Q	Electric charge at a branch i.e. at a component
q	Charge variable conjugate to a node flux variable
re	Real part
S_{ji}	Scattering parameter between input port i and output port j
T	Temperature
T_1	Lifetime of the qubit
T_2^*	Ensemble-averaged dephasing time of the qubit
$\hat{T}(y)$	Translation operator that takes the state $\|x\rangle$ to $\|x+y\rangle$
u	Amplitude of a quantum state
$u_n(\varphi)$	Solution to Mathieu's equation
V	Voltage
Z_0	Characteristic impedance
α	Anharmonicity of a multilevel system
$\boldsymbol{\beta}$	A list of fit parameters
γ	Decay rate of a qubit excitation
Δ	Superconductor energy gap parameter
θ	Phase of a quantum state
κ	Decay rate of a resonator
λ	Analytic model function for fitting
$\hat{\rho}$	Density operator of a system
$\boldsymbol{\Sigma}$	Covariance matrix
$\sigma^2(x)$	Variance of a variable x
$\boldsymbol{\sigma}$	Vector of Pauli operators, with components $\hat{\sigma}_1 = \|e\rangle\langle g\| + \|g\rangle\langle e\|$, $\hat{\sigma}_2 = i\left(\|e\rangle\langle g\| - \|g\rangle\langle e\|\right)$, $\hat{\sigma}_3 = \|g\rangle\langle g\| - \|e\rangle\langle e\|$
Φ	Branch flux: the time integral of voltage across a two-port component
Φ_0	Magnetic flux quantum, $h/(2e)$
ϕ	Node flux: the sum of branch fluxes from the ground potential to a node
φ	Difference in the phases of two superconducting order parameters
χ	Dispersive shift
$\chi_{i,j}$	Partial dispersive shift related to qubit transition between states i and j
$\Psi(\mathbf{r}, t)$	Phenomenological order parameter of a superconducting ground state
ω	Angular frequency

Contents

Chapter 1

Introduction

Quantum mechanics currently constitutes the most accurate description of matter at tiny scales comparable to the so-called de Broglie wavelength of the studied objects, and at nonrelativistic energies. As the general understanding of the subject has matured for a century, the focus of study has shifted from comprehension towards control. A *universal quantum computer* is a Turing machine in which classical bits are replaced by quantum mechanical two-state systems, *qubits* [1]. Logic gates are implemented with controlled unitary time evolution of the qubits. Experimental requirements for realizing such a system are listed by the so-called DiVincenzo criteria [2]. Since Feynman proposed the idea in the 1980's [3], the implementation of a quantum computer has proven to be a great challenge. To date, there exist no large-scale universal quantum computers. However, there has been promising and steady experimental progress . As of today, the latest steps towards the elusive machine include *quantum-enhanced computers* that use a quantum-annealing-based device to solve optimization problems in an otherwise classical computer [4], as well as small-scale universal quantum circuit boards [5].

Although a classical computer, when given enough time, is capable of solving every problem that a full-fledged quantum computer would, efficiency is the hoped-for relish in quantum computing. Algorithmic efficiency is determined by how the computational time, i.e. the number of computational steps, increases as a function of the input size. Some problems can be solved by algorithms that grow slower at most as a polynomial of a constant degree. For others, only less efficient algorithms are known that slow down e.g. exponentially. Typically in computer science, polynomial or higher efficiency is considered efficient, and anything worse as inefficient.

This is the sense in which quantum computers promise to be useful: by solving efficiently problems that are solved only inefficiently by a classical machine. The gain in efficiency is due to *coherent superposition* of quantum states, and the so-called *entanglement* between them. In a quantum computer, a memory register of length n is represented by a quantum state consisting of n qubits. Each qubit is at a state labeled by zero or one, or at a superposition or a mixture of these. As a qubit can be in a superposition of e.g. all possible basis states, in some sense it is possible to compute all values of a function

simultaneously i.e. in parallel, using many-qubit-states. Of course, each measurement yields only one of the values. Nonetheless, *quantum parallelism* may be exploited with clever algorithms that provide e.g. probability distributions in which output states yielding the solution of the problem at hand have higher probabilities of occurring. Quantum Fourier transforms [6], [7], quantum search algorithms [8], [9] and quantum simulation [10], which are the only known useful classes of algorithms that outperform classical algorithms, all depend on quantum parallelism to some extent in reducing the number of computation steps. In fact, it is still a considerable challenge to design algorithms that take the most out of the quantum nature of the proposed machines, and utilization of the quantum degrees of freedom is not always efficient.

Another major problem, *decoherence*, arises from the fragile nature of the coherent superpositions. Quantum states evolve into classical statistical mixtures of zeros and ones when they interact with the surroundings. Decoherence [11] both introduces errors in the final states and destroys the quantum nature of the qubits. This limits the time a qubit can be fruitfully used in a continuous set of calculations, that is, computation without error correction [12]. None of the available implementations strictly reach the needed threshold. Acceptable error rate per quantum gate depends on employed error models, but usually 10^{-4} is taken as the guideline [13]. In addition to developing error correction methods, improving the design of the qubits as well as the architecture of the quantum computer is crucial in reaching the threshold.

There is a long list of proposals for qubits as well as for the architecture of the quantum computer. This thesis focuses on superconducting quantum computers, in which nonlinear electric components, the qubits, are operated with microwave photons inside transmission-line resonators. Other noteworthy realizations include cavity-trapped ions [14], [15]; spins in silicon dopants [16] or quantum dots [17], operated with magnetic fields; optical photons operated with linear optical elements [18], [19]; and topological quantum computers [20]. Superconducting qubits are attractive because their parameters are highly tunable, they are affordably scalable and readily integrable with parts of existing electric circuits. As a downside, their coherence times are somewhat shorter than those of some rivaling realizations. However, as coherence times have increased, they are no longer considered to be the limiting factors. Among superconducting qubits, transmission-line-shunted plasma oscillation qubits, or *transmons*, are one of the most promising ones [21].

The purpose of this thesis is to present experimental methods for measuring superconducting qubits, and to provide an overview of the related theory. Chapters 2 and 3 together provide theoretical background and context for superconducting qubits. Chapter 2 reviews the Lagrangian formalism and canonical quantization procedure for electric circuits. Taking the quantum transmon Hamiltonian derived in Chapter 2, Chapter 3 derives perturbative and limiting results, as well as approximate analytic eigenvalues for a system of a qubit and two resonators, connecting the transmon system into more re-

alistic experimental regime and setting. Chapter 4 records the cryogenic measurement scheme and statistical methodology. Chapter 5 presents the main experimental results and data analysis. The experiments explore phenomena at the center of circuit Quantum Electrodynamics (cQED). The qubit-resonator coupling constants, the Josephson energy and charging energy of the qubit are determined via steady state measurement of the transmission coefficient, while the coherence times are measured by employing pulse-modulation. Relevant statistical uncertainties are determined with Monte Carlo (MC) pseudo experiments. Experimental results are provided for a single transmon sample, which is designed and fabricated in ETH, Zurich.

Chapter 2

Theoretical background

After a brief review of quantum mechanics of qubits, in this Chapter, we quantize the degrees of freedom of the transmon. This is achieved in a formalism which combines tools from the canonical quantization procedure and the basics of electric circuit analysis. The analogy between interacting quantum fields and electromagnetic circuits is already mentioned in the classic textbook on relativistic quantum fields [22]. Ref. [23] presents a procedure for obtaining the Lagrangian of a circuit, especially focusing on transmission lines. We mostly follow the review given in Ref. [24], as well as the more recent version of this review [25]. The transmon consists of several components, which are first considered separately is Secs. 2.2.2, 2.2.3, and 2.2.4. In Sec. 2.2.5, we couple the components and carry out the quantization to obtain the transmon Hamiltonian operator.

2.1 Two-state systems as quantum bits

A quantum-mechanical *two-state system* is related to an observable with two eigenvalues. The orthonormal eigenstates of such an observable, $|0\rangle$ and $|1\rangle$, form a complete basis in a two-dimensional Hilbert space. This basis is sometimes called the logical basis. Unless otherwise specified, we work in this basis. When the observable is the qubit Hamiltonian $\hat{H}$, $|0\rangle$ is typically the ground state and $|1\rangle$ the excited state. These states are also denoted by $|g\rangle$ and $|e\rangle$ to emphasize that only the two lowest excitations are considered, and to notationally separate the qubit states from other systems. Any quantum state of an isolated two-state system can be expressed [26] as

$$|\psi\rangle = \sin(x/2)|0\rangle + \cos(x/2)e^{iy}|1\rangle. \tag{2.1}$$

The state evolves according to the Schrödinger equation $i\hbar\partial_t|\psi\rangle = \hat{H}|\psi\rangle$. In Eq. (2.1) the unmeasurable, global phase factor common to both eigenstates is chosen to be 1. The phase difference y reflects the inherent quantum properties of the system, which, for example, involve nonclassical probability distributions.

The effective state of an individual qubit coupled to other systems may always be

written in terms of a *density operator*, which, in the logical basis, is given by

$$\hat{\rho} = \rho_{00}|0\rangle\langle 0| + \rho_{01}|0\rangle\langle 1| + \rho_{01}^{*}|1\rangle\langle 0| + \rho_{11}|1\rangle\langle 1|, \tag{2.2}$$

where $\rho_{ij} \in \mathbb{C}$, and $\rho_{00} + \rho_{11} = 1$. The density operator is positive semi-definite. For *pure states*, defined by $\mathrm{tr}\left(\hat{\rho}^2\right) = 1$, the density operator is an equivalent description to the state vector (Eq. (2.1)), with the correspondence $\hat{\rho} = |\psi\rangle\langle\psi|$. If the quantum state of the whole system is known, the qubit density operator is obtained by taking the partial trace, tracing out the degrees of freedom of the other subsystems. If the qubit does not entangle with the other subsystems, the state of the qubit remains pure. While the state representation (Eq. (2.1)) often leads to a more simple description, the advantage in the density operator representation is that it is always valid.

The diagonal elements of $\hat{\rho}$ correspond to the populations, i.e. the probabilities of finding the qubit in the ground or excited state. The off-diagonal elements measure *coherence*, i.e. deviation from a classical two-state system in the following sense. Let us measure an observable $\hat{A}$ with eigenvalues a and eigenstates $|a\rangle$. According to the laws of quantum mechanics [26], the probability to observe a is given by the expression

$$\begin{aligned}\mathcal{P}(a) &= \langle a|\hat{\rho}|a\rangle \\ &= \rho_{00}|\langle 0|a\rangle|^2 + \rho_{01}\langle 0|a\rangle\langle a|1\rangle + \rho_{01}^{*}\langle 1|a\rangle\langle a|0\rangle + \rho_{11}|\langle 1|a\rangle|^2 \\ &= \mathcal{P}(a|0)\mathcal{P}(0) + \mathcal{P}(a|1)\mathcal{P}(1) + \rho_{01}\langle 0|a\rangle\langle a|1\rangle + \rho_{01}^{*}\langle 1|a\rangle\langle a|0\rangle,\end{aligned}$$

where $\mathcal{P}(i|j)$ refer to conditional properties of getting a result i for a qubit in the state $|j\rangle$. If the off-diagonal elements are zero, the last two terms drop out. What is left is a classical probability distribution for $\hat{A}$. As an example, for the state of Eq. (2.1), $\rho_{01} = \sin(x/2)\cos(x/2)e^{-iy}$, which vanishes if either $\sin(x/2)$ or $\cos(x/2)$ is zero, which is the case when the qubit is entirely in either the ground or excited state. Furthermore, the term averages over time to zero if y is random at different times.

The state of a qubit may also be visualized with the help of a *Bloch vector*, which is a unit vector on a sphere, $\mathbf{n} = (\cos(y)\sin(x), \sin(y)\sin(x), \cos(x))$. The Bloch vector yields the decomposition

$$\hat{\rho} = \frac{1}{2}\left(\mathbf{I} + n_i\hat{\sigma}_i\right), \tag{2.3}$$

where $\hat{\boldsymbol{\sigma}} = (\hat{\sigma}_x, \hat{\sigma}_y, \hat{\sigma}_z)$ are the Pauli operators, and the angles are defined by Eq. (2.1). In terms of the density matrix (Eq. (2.2)), the Bloch vector has the components

$$n_x = \rho_{01} + \rho_{01}^{*},\ n_y = i\left(\rho_{01} - \rho_{01}^{*}\right),\ n_z = \rho_{00} - \rho_{11}. \tag{2.4}$$

The states $|0\rangle$ and $|1\rangle$ correspond to the north and south poles. The Pauli operators $\hat{\sigma}_z$ and $\hat{\sigma}_x$ are generators to transformations which rotate the Bloch vector around z- or x-axes. In

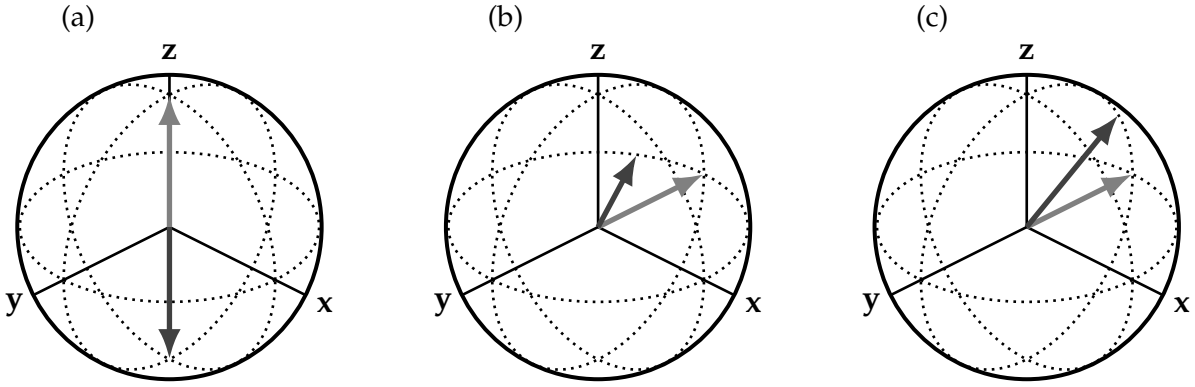

Figure 2.1: **Qubit states on a Bloch Sphere.** The basis states $|0\rangle$ and $|1\rangle$ are illustrated in (a). The state $(|0\rangle - i|1\rangle)/\sqrt{2}$ before (lighter arrow) and after (darker arrow) acted on by a rotation involving (b) $\hat{\sigma}_3$ and (c) $\hat{\sigma}_1$, respectively.

fact, unitary time evolution can be expressed in terms of these Pauli operators.[1] See Fig. 2.1 for pictorial representation of the Bloch vectors before and after rotations generated by the Pauli operators.

In practice even the most elementary systems, such as electrons, have several measurable properties, Σ, in addition to their two-state observables and hence, their full state is described by $|\psi, \Sigma\rangle$ instead of $|\psi\rangle$. However, this poses no problem as long as these degrees of freedom do not entangle with the two-state part. Furthermore, apart from the spin of spin-1/2 particles, natural two-state systems are rare. Fortunately, many n-state systems may be described as two-state systems provided that they are sufficiently *anharmonic*. That is, $E_i - E_1 \neq E_1 - E_0$, where E_i is the energy eigenvalue of the ith state. Thus, transitions between e.g. $|g\rangle$ and $|e\rangle$ can be driven without driving transitions between states i and k. Theoretically, any non-zero degree of anharmonicity would do, but in practice the band of a driving frequency has a finite width. Larger anharmonicity is more useful to allow for greater changes in the driving pulse.

2.2 Quantization of circuit elements

A traditional quantization procedure begins with identifying the necessary canonical degrees of freedom. Since voltage and current through the electric circuit define the energy stored in it, it is not unnatural that the time integrals

$$\Phi(t) = \int_{-\infty}^{t} dt' \, V(t'), \tag{2.5}$$

$$Q(t) = \int_{-\infty}^{t} dt' \, I(t'), \tag{2.6}$$

[1] Because of the identity $\sigma_i \sigma_j = \delta_{ij}\mathbf{I} + \sum_k 2i\epsilon_{ijk}\sigma_k$, where ϵ_{ijk} is the Levi-Civita symbol, operation with $\hat{\sigma}_y$ is a combination of operations with $\hat{\sigma}_x$ and $\hat{\sigma}_z$.

represent variables analogous to position and momentum of a moving particle in Lagrangian formalism [27], [24], for each component in the circuit. Here, Φ and Q are the flux[2] and charge, defined by the voltage, V, and the current, I, across the ports of the component. Following the convention in [24], voltage increases in the opposite direction of the current. Note that Eq. (2.5) agrees with Maxwell-Faraday equation,

$$\dot{\Phi} = V, \tag{2.7}$$

an identity which we will use frequently. Networks of electric components may be described in terms of *branches* and *nodes*, that is of two-port components and oriented lines that connect them. The orientation of a node is equal to the direction of the current. In a lumped-element model, where voltage and current are uniform across a conductor at an instant of time, a node is a region of uniform electric potential. Flux and charge of Eqs. (2.5) and (2.6) are defined for each branch. However, Kirchhoff's laws for voltage around a loop and current at a node,

$$\sum_{\dot{Q}_b \text{ coming into } n} \dot{Q}_b = 0, \tag{2.8}$$

$$\sum_{\Phi_b \text{ around } l} \Phi_b = \tilde{\Phi}, \tag{2.9}$$

reduce the number of independent degrees of freedom. The sum in Eq. (2.8) is taken over positive current that enters or negative current that leaves a node, from branches that are immediately connected to node n. Similarly, the sum in Eq. (2.9) expands over the branch fluxes around a loop l. The sum is equal to a static constant $\tilde{\Phi}$.

There is a systematic, although not unique, way to choose the dynamical degrees of freedom [24]. The procedure begins with a naming convention: one of the nodes is chosen to be *ground*. Nodes which are only connected to capacitive branches are referred to as *passive*, and the remaining ones as *active*. Let *tree* be a network of a subset of branches and the nodes these branches touch. In a *spanning tree*, the subset of branches is such that every node of the circuit belongs to the tree, but there are no loops, that is, closed cycles, within the network of the tree. See Fig. 2.2 for examples. The branches not in the spanning tree form the set of so-called closure branches, also known as the co-spanning tree. There may be several possible spanning trees for a single circuit. One of them is chosen, and either the branch fluxes or charges of the spanning branches supply the dynamical coordinate degrees of freedom. We choose the flux variables as the coordinate variables.

It is conventional to re-express the associated variables with node variables, denoted with non-capital ϕ. The *node flux* is defined as the oriented sum of branch fluxes along a path from ground to the node in question. Conversely, the branch flux is obtained as the

[2]The flux has units of magnetic flux. It is also referred to as the magnetic flux linkage, since it is not always equal to the magnetic flux through a surface, for example, in the case of a memristor.

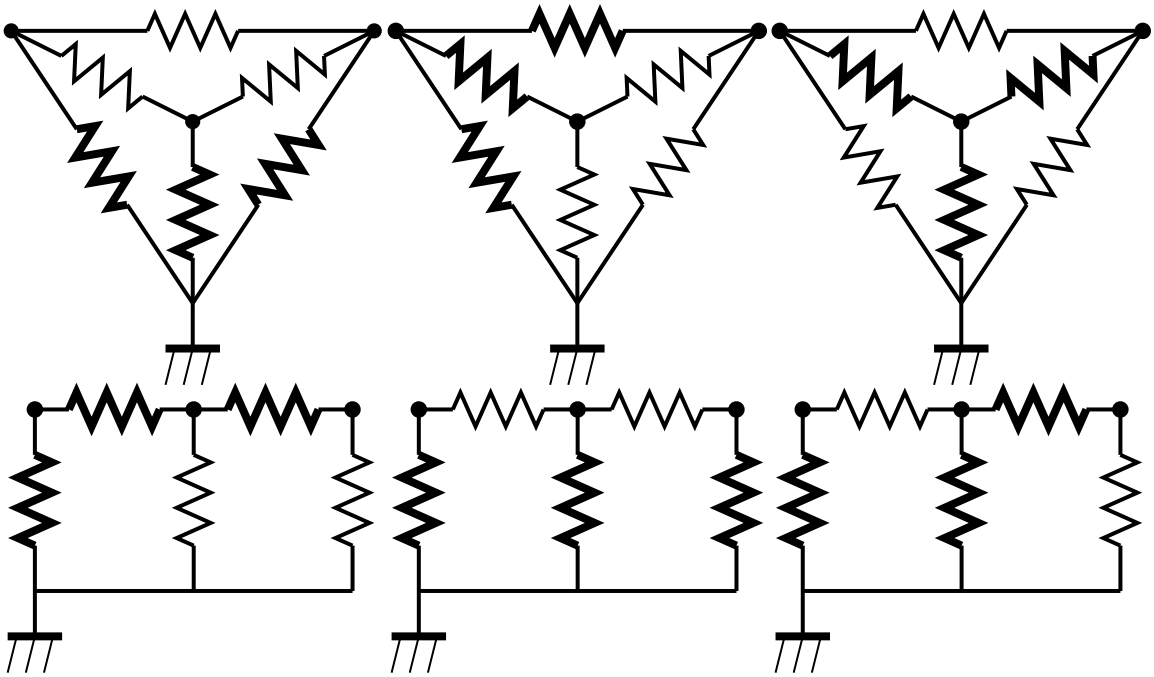

Figure 2.2: **Spanning trees.** Examples of spanning trees of circuits of two different topologies. Spanning tree branches are bolded, while closure branches are not. Nodes other than the ground are denoted with bold circles, while the fork symbol indicates the ground node.

difference of node fluxes across it, as

$$\Phi_b = \phi_{n_{\text{before}}} - \phi_{n_{\text{after}}}, \tag{2.10}$$

$$\Phi_{b'} = \phi_{n_{\text{before}}} - \phi_{n_{\text{after}}} + \tilde{\Phi}, \tag{2.11}$$

where $\tilde{\Phi}$ is the constant flux through the loop, as given by Eq. (2.9). Here, Φ_b is part of the spanning tree, while $\Phi_{b'}$ belongs to closure branches. In Lagrangian mechanics, the other degree of freedom besides the coordinate is the time-derivative of the coordinate, $\dot{\phi}_n$. Specifying the coordinate variables also determines the conjugate variables of Hamiltonian mechanics.

The Lagrangian function, L, is obtained as the difference of the kinetic and the potential energies. Electric component energies are obtained by integrating the power $P = VI$ with respect to time. The circuit elements considered in this thesis are either capacitive, inductive, or voltage sources. Capacitive element stores charge as a function of voltage across them. That is, there is a relation of the form

$$Q = g(\dot{\Phi}), \tag{2.12}$$

or $\dot{\Phi} = g^{-1}(Q)$ for some smooth function g. Here, Q is the positive charge accumulated on the plate with the relative negative potential. Voltage sources are approximated as capacitors, for which $Q_s/C_s = V$, and $C_s \to \infty$ [24]. The capacitive energy term that

corresponds to a voltage source is a constant of motion and does not contribute to the equations of motion. The voltage sources considered are coupled capacitively to the rest of the circuit with a so-called gate-, or input-port-capacitor, and contribute to the total energy through the charging of the gate capacitor. Inductive elements induce a flux according to a relation

$$\Phi = h(\dot{Q}), \tag{2.13}$$

or $\dot{Q} = h^{-1}(\Phi)$ for some smooth function h. Here, $\dot{Q}$ is the current that induces the flux. Relations (2.7), (2.12) and (2.13) enable us to express the power across a component in terms of Q, Φ or their time-derivatives.

Owing to the choice of ϕ_n as the coordinate, capacitive energies have the forms of kinetic energies, while inductive energies represent potential terms. Lagrangian provides the equations of motions for the active node fluxes and their derivatives, as well as the conjugate variables

$$q_n = \frac{\partial L}{\partial \dot{\phi}_n}. \tag{2.14}$$

referred to as node charges. Note that for passive nodes, $q_n = 0$. Consequently, passive nodes are not considered to be dynamical degrees of freedom. The Hamiltonian H of a system is obtained by Legendre transforming the Lagrangian, as $H = \sum_n q_n \dot{\phi}_n - L$, where the sum is taken over active nodes.

In quantum mechanics, the canonical degrees of freedom are promoted to hermitian operators

$$\phi_n \to \hat{\phi}_n,$$
$$q_n \to \hat{q}_n,$$

which are defined to obey the canonical commutation relation

$$[\hat{\phi}_n, \hat{q}_n] = i\hbar,$$

where $\hbar$ is the reduced Planck constant. This commutation relation implies that the operators do not have any mutual eigenstates. Although one might argue it is counterintuitive to start from a classical description and end up with a more precise quantum mechanical one, this procedure is known to produce the correct results.

2.2.1 Mathematica implementation

The procedure of obtaining the capacitive part of the classical Hamiltonian of a given circuit is implemented with Mathematica and can be found on github[3]. Circuit graphs are

[3] github.com/patomaki/cQEDNetworks

implemented as directed graphs, most properties of which are read from the incidence matrix of the graph. In addition to the incidence matrix, the user provides lists of branch and node labels, branch types and symbolic capacitances. The implementation consists of a Mathematica package, which contains a set of functions for finding the cycles, spanning trees, and associated co-spanning trees of a given circuit graph, as well as functions for classifying nodes as ground, passive and active, for symbolically performing the change of variables from branch to node variables, and related helper functions. In an additional Mathematica notebook, included to provide an usage example, these functions are used for symbolically calculating the capacitive Lagrangian for the appropriate degrees of freedom, the associated conjugate charges, and subsequently, the capacitive Hamiltonian as a function of the conjugate charges. Examples are provided for the Cooper pair box and for the transmon.

2.2.2 LC oscillator

A coplanar waveguide (CPW) consists of a long strip forming the center conductor, which is located between the ground planes. It is well known that a CPW resonator acts as a LCR oscillator when driven near its resonance frequency ω_r [28]. This is because at resonance, modes of standing electromagnetic waves are formed inside the resonator, such that energy oscillates between the electric and the magnetic field. Since the resonant modes are determined by the length of the CPW, the qubit may be placed at a location where it only strongly interacts with odd or even modes of the resonator. At temperatures well below the critical temperature of the conductor used in the CPW, the resonator can be rather accurately modelled as an LC oscillator, i.e., a linear circuit with a capacitor and an inductor in series.

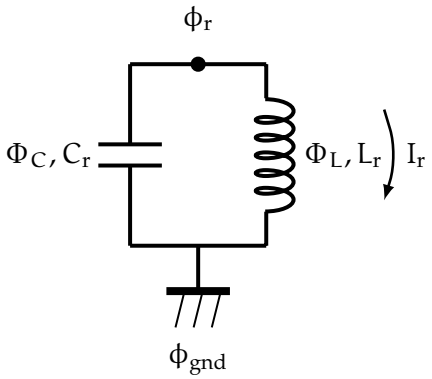

Figure 2.3: LC **oscillator circuit**. The capital symbols Φ_C and Φ_L denote branch fluxes, and ϕ_r and ϕ_{gnd} represent node fluxes. The black dot indicates the active node, and the arrow the positive direction of the current.

See Fig. 2.3 for a circuit diagram of an LC oscillator, where the variables Φ_C and Φ_L denote the fluxes through the inductor and across the capacitor. Choosing zero total flux around the circuit, Kirchhoff's law in (Eq. (2.9)) affirms that $\Phi_C = -\Phi_L$. Taking

the inductor as the closure branch, we take $\Phi_r := \Phi_C$ as the independent flux variable. Linearity of the components implies that the relations (2.12) and (2.13) assume the forms

$$Q = C_r \dot{\Phi}_r, \tag{2.15}$$

$$\Phi_r = L_r \dot{Q}, \tag{2.16}$$

for some constants C_r and L_r. Here, Q is the charge accumulated on the capacitor plate on the active node side. The capacitive energy term is conviniently found in terms of the charge, by integrating the power it takes to load the capacitor, with respect to time

$$\begin{aligned} T &= \int_{-\infty}^{t} dt' \, \frac{Q}{C_r} \dot{Q} \\ &= \int_0^Q dQ \, \frac{Q}{C_r} \\ &= \frac{Q^2}{2C_r}. \end{aligned}$$

Relation (2.15) allows to express the capacitive energy in terms of the flux variable, as

$$T = \frac{C_r \dot{\Phi}_r^2}{2}. \tag{2.17}$$

The inductor contributes the energy term

$$\begin{aligned} U &= \int_{-\infty}^{t} dt' \, \dot{\Phi}_r \frac{\Phi_r}{L_r} \\ &= \int_0^{\Phi_r} d\Phi_r \, \frac{\Phi_r}{L_r} \\ &= \frac{\Phi_r^2}{2L_r}. \end{aligned} \tag{2.18}$$

Conversion to node variables is swift, since $\Phi_r = \phi_r - \phi_{gnd} = \phi_r$ for $\phi_{gnd} = 0$. The Lagrangian is given by the difference

$$\begin{aligned} L &= T - U \\ &= \frac{C_r \dot{\phi}_r^2}{2} - \frac{\phi_r^2}{2L_r}. \end{aligned}$$

Partial derivation reveals the conjugate variable

$$q_r := \frac{\partial L}{\partial \dot{\phi}_r} = C_r \dot{\phi}_r,$$

which is the accumulated charge charge Q in Eq. (2.15). Legendre transforming L with

$q_r\dot{\phi}_r$ we obtain the textbook Hamiltonian

$$H = \frac{q_r^2}{2C_r} + \frac{\phi_r}{2L_r}. \tag{2.19}$$

Promoting q_r and ϕ_r into quantum operators we observe that the LC oscillator is a quantum harmonic oscillator, which is defined by the Hamiltonian operator

$$\hat{H} = \frac{\hat{q}_r^2}{2C_r} + \frac{\hat{\phi}_r^2}{2L_r}. \tag{2.20}$$

In Ref. [29], a one-dimensional transmission-line resonator is modelled as an infinite set of LC oscillators, which is a general approach for circuit elements with impedance [24]. The resulting Hamiltonian corresponds to a set of harmonic oscillators. The Hamiltonian of Eq. (2.20) is diagonalized by the non-hermitian *ladder operators*

$$\hat{a} = \sqrt{\frac{Z}{2\hbar}}(\hat{\phi}_r + iZ\hat{q}_r), \tag{2.21}$$

$$\hat{a}^\dagger = \sqrt{\frac{Z}{2\hbar}}(\hat{\phi}_r - iZ\hat{q}_r), \tag{2.22}$$

where $Z = (L_r/C_r)^{1/2}$ is the *characteristic impedance* of the oscillator. In terms of the ladder operators,

$$\hat{H} = \hbar\omega_r(\hat{a}^\dagger\hat{a} + 1/2), \tag{2.23}$$

where $\omega_r = (L_rC_r)^{-1/2}$ is the angular frequency of the oscillator. If we define *vacuum* as the state $|0\rangle$, which satisfies $\hat{a}|0\rangle = 0$, the rest of the eigenstates, $|E_n\rangle := |n\rangle$, $n \in \mathbb{N}$, are given by

$$|n\rangle = \frac{(\hat{a}^\dagger)^n}{\sqrt{n!}}|0\rangle,$$

which may be checked by inserting the states $|n\rangle$ into the eigenvalue problem $\hat{H}|E_n\rangle = E_n|E_n\rangle$. The corresponding eigenvalues are $E_n = \hbar\omega_r(n + 1/2)$. Each ladder operator corresponds to adding or removing one quantum of energy from the system.

The energy quanta of the LC oscillator are photons [30]. They are certainly bosonic, because the ladder operators satisfy $[\hat{a}, \hat{a}^\dagger] = 1$. The degrees of freedom of the quantized charge and flux can also be expressed in terms of the electric field between the capacitor plates, and magnetic field through the inductor. Thus the LC oscillator describes a quantized electromagnetic field inside the LC oscillator, the excitations of which are photons.

2.2.3 Cooper pair box

The Cooper pair box (CPB), presented as a circuit diagram in Fig. 2.4, consists of a capacitively shunted Josephson junction and a gate capacitor that can be used to attract Cooper pairs on the superconducting island between the two components. For the purpose of this section, a Josephson junction is a lossless nonlinear inductor in parallel with a capacitor. An introduction to Josephson junctions is given in Appendix A.

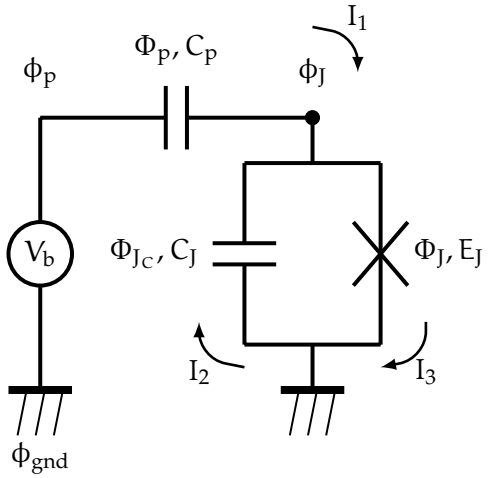

Figure 2.4: **Cooper pair box equivalent circuit**. The cross represents the nonlinear inductor of the Josephson junction. Capital symbols indicate branch variables, and non-capital symbols indicate node variables. The black dot indicates the active node, and the arrows indicate the directions of the currents. The bias voltage source is denoted with the component labeled by V_b.

Flux across the input capacitor is denoted with Φ_p. Likewise, Φ_J and Φ_{J_C} refer to fluxes across the Josephson junction tunnelling element and capacitor. The input port and the Josephson junction capacitor are chosen as closure branches, which leaves the branch fluxes of the Josephson junction inductor and the voltage source as the spanning branches. Kirchhoff's law (2.9) implies the relations

$$\begin{aligned} \Phi_{J_C} &= -\Phi_J, \\ \Phi_p &= -\Phi_J - \Phi_b. \end{aligned}$$

In terms of node variables (see Eq. (2.10)),

$$\begin{aligned} \Phi_J &= -\phi_J + \phi_{gnd} = -\phi_J, \\ \Phi_b &= \phi_p - \phi_{gnd} = \phi_p, \\ \Phi_p &= \phi_J - \phi_p, \end{aligned}$$

where the latter equalities hold assuming $\phi_{gnd} = 0$. This justifies the use of the same label for both the Josephson junction branch and the island node. For a Josephson junction, the

relations of the form of Eqs. (2.12) and (2.13) are given by the *Josephson relations* [31]

$$I_3 = I_c \sin(\varphi), \tag{2.24}$$

$$V_J = \frac{\hbar}{2e}\dot{\varphi}. \tag{2.25}$$

Here, I_c is the critical current, which is adjustable in fabrication. If a current higher than the critical current is forced through the junction, the voltage rises above a threshold of $2\Delta/e$, exciting non-paired electrons, often referred to as quasiparticles[4] in this context. Here, Δ is a material specific gap parameter of the superconductor. In this thesis, we only consider currents below critical currents. The variable φ is the order parameter phase difference across the junction and V_J is the voltage across the junction. See Appendix A for a more precise definition of φ, as well as a theoretical background for the relations (2.24) and (2.25). The ac relation (2.25) together with Eq. (2.7) implies that $\dot{\varphi} = \dot{\Phi}_J\, 2e/\hbar$. Consequently, φ and Φ_J are related by

$$\varphi = \frac{2e}{\hbar}\Phi_J = 2\pi\frac{\Phi_J}{\Phi_0}, \tag{2.26}$$

apart from an irrelevant additive constant. The inductive energy related to the junction is given by

$$\begin{aligned} U_J &= \int_{-\infty}^{t} dt'\, V_J I_3 \\ &= \int_0^{\varphi} d\varphi' \frac{\hbar I_c}{2e}\sin(\varphi') \\ &= -\frac{\hbar I_c}{2e}\cos(\varphi) + \frac{\hbar I_c}{2e}, \end{aligned} \tag{2.27}$$

where the constant $\hbar I_c/2e$ is ignored in what follows. For notational simplicity, it is customary to define the *Josephson energy* as $E_J = \hbar I_c/(2e)$. It can be approximated by the Ambegaokar–Baratoff relation

$$E_J = \frac{1}{2}\frac{\hbar}{2\pi(2e)^2}G\Delta,$$

where G is the normal-state conductance of the junction. Using the capacitive energy calculated for the LC oscillator, the energies of the input port capacitor and the junction capacitor are readily written as

$$T_p = \frac{C_p\dot{\Phi}_p^2}{2} = \frac{C_p(\dot{\phi}_J - V_b)^2}{2},$$

$$T_J = \frac{C_J\dot{\Phi}_J^2}{2} = \frac{C_J\dot{\phi}_J^2}{2}.$$

[4] These electrons behave differently from electrons in conductors which are completely normalconducting [32].

As discussed, we model the voltage source as a capacitor with $Q_b/C_b = V_b$, and $C_b \to \infty$. In this approximation, ϕ_p is a passive node. Thus, the voltage source also formally contributes a capacitive term, which is ignored here, as it is a constant of motion. In this approximation, the CPB Lagrangian becomes

$$\begin{aligned} L &= T_p + T_J - U_J \\ &= C_J \frac{\dot{\phi}_J^2}{2} + C_p \frac{(\dot{\phi}_J - V_b)^2}{2} + E_J \cos\left(2\pi \frac{\phi_J}{\Phi_0}\right). \end{aligned}$$

As the island node is the only active node, the only conjugate momentum is given by

$$q_J = \frac{\partial L}{\partial \dot{\phi}_J} = \left(C_J + C_p\right)\dot{\phi}_J - C_p V_b,$$

Consequently, the Hamiltonian of the CPB becomes

$$\begin{aligned} H &= q_J \dot{\phi}_J - L \\ &= \frac{(q_J + C_p V_b)^2}{2(C_p + C_J)} - E_J \cos\left(2\pi \frac{\phi_J}{\Phi_0}\right) - \frac{1}{2} C_p V_b^2, \end{aligned}$$

where the term $\propto C_p V_b^2$ only shifts the Hamiltonian by an unobservable offset, which is ignored. The active node variables are quantized, as

$$\begin{aligned} \phi_J &\to \hat{\phi}_J \\ q_J &\to \hat{q}_J. \end{aligned}$$

We also enforce

$$[\hat{\phi}_J, \hat{q}_J] = i\hbar. \tag{2.28}$$

Furthermore, it is conventional to introduce the number of Cooper pairs on the island, $\hat{n} = \hat{q}_J/(-2e)$, and the dimensionless *gate charge*, $n_g := -C_p V_b/(-2e)$, which is the contribution of the input port voltage to the number of Cooper pairs on the input port capacitor, also known as gate capacitor. As a function of these and the phase operator $\hat{\varphi}$, which is related to $\hat{\phi}_J$ via Eq. (2.26), the CPB Hamiltonian assumes the form

$$\begin{aligned} \hat{H} &= (-2e)^2 \frac{(\hat{n} - n_g)^2}{2\left(C_J + C_p\right)} - E_J \cos\left(\hat{\varphi}\right) \\ &= f4E_C \left(\hat{n} - n_g\right)^2 - E_J \cos\left(\hat{\varphi}\right), \end{aligned} \tag{2.29}$$

where *charging energy* $E_C = e^2/[2(C_J + C_p)]$. It follows from Eq. (2.28) that the dimension-

less variables $\hat{n}$ and $\hat{\varphi}$ satisfy the commutation relation

$$[\hat{n}, \hat{\varphi}] = i.$$

For the properties of the phase operator, and for references, see Appendix B.

In the Cooper pair number basis, an analytical solution is not known. However, in the phase basis $\{|\varphi\rangle\}$, where $\langle\varphi|\hat{\varphi}|\varphi'\rangle = \delta(\varphi - \varphi')$ and $\hat{n} \hat{=} i\partial_{\hat{\varphi}}$, there is an analytical solution for the stationary states in terms of certain special functions. By defining a function $u_m(\varphi)$ such that $\psi_m(\varphi, n_g) = e^{in_g\varphi}u(\varphi/2)$, where ψ_m satisfies $H\psi_m(\varphi, n_g) = E_m\psi_m(\varphi, n_g)$, the eigenvalue equation reduces to the *Mathieu's equation*

$$\frac{d^2u_m(\varphi)}{d\varphi^2} - \left[\frac{4E_m}{E_C} + \frac{4E_J}{E_C}\cos(2\varphi)\right]u_m(\varphi) = 0 \tag{2.30}$$

for $u_m(\varphi)$. If we interpret Eq. (2.30) as an eigenvalue equation for $u_m(\varphi)$, the corresponding Hamiltonian operator is π-periodic. The Hamiltonian thus commutes with the translation by π, $\hat{T}(\pi)$. This further implies that the eigenstates of the Hamiltonian may simultaneously be chosen as the eigenstates of $\hat{T}(\pi)$. That is, $T(\pi)u_m(\varphi) = e^{i\xi\pi}u_m(\varphi)$ for some ξ. According to Bloch's theorem, this is equivalent with that u_m satisfies $u_m(\varphi) = e^{i\xi\varphi}v_m(\varphi)$ for some π-periodic function $v_m(\varphi)$. This identity together with the boundary condition $\psi_m(\varphi) = \psi_m(\varphi + 2\pi)$ dictate that $\xi = -2n_gk$ for some integer k. This is the approach employed in [33], where it is stated that k and the energy levels E_m are given by

$$\begin{aligned} k_m &= \mathrm{mod}\left[\mathrm{int}(2n_g - 1/2), 2\right] \times \{\mathrm{int}(n_g) - (-1)^m\mathrm{div}(m+1, 2)\} \\ &\quad + \mathrm{mod}\left[\mathrm{int}(2n_g + 1/2), 2\right] \times \{\mathrm{int}(n_g) + (-1)^m\mathrm{div}(m+1, 2)\}, \\ E_m &= E_C\,\mathrm{ma}_{2(n_g - k_m)}\left[-E_J/(2E_C)\right]. \end{aligned} \tag{2.31}$$

Here, $\mathrm{mod}(x, y)$ is the modulo operation, $\mathrm{int}(x)$ chooses the integer closest to x and $\mathrm{div}(x, y)$ gives the integer quotient of x and y in the division of x by y. For example, $\mathrm{int}(1.23) = 1$, $\mathrm{mod}(12, 5) = 2$ and $\mathrm{div}(7, 3) = 2$. Furthermore, ma is the special function *Mathieu's characteristic a*. It does not have a simple form, but it is implemented into symbolic calculators such as *Mathematica* and *Maple*. The n_g-dependence of the energy levels plays a role in the definition of a transmon type qubit.

The u_m relevant to this problem are found as linear combinations of Mathieu's cosine and sine functions for $n_g \in]0, 1/2[$ [34]. They are special functions that lack simple forms, and they will not be needed in this thesis. For $n_g \in \mathbb{R}$, it is formally possible to solve the Taylor coefficients of u_m in Eq. (2.30). However, the Taylor series cannot be restricted to solutions that satisfy Bloch's theorem, because a periodicity condition will give a constraint where the ith Taylor coefficient depends on every Taylor coefficient in the series.

2.2.4 Direct current superconducting interference device

A direct current superconducting interference device (dc SQUID) is obtained by replacing the Josephson junction of a CPB with two Josephson junctions that form a supercurrent loop. This loop can be threaded by a bias magnetic flux Φ. Then, the fluxes around the junctions, Φ_{J_1} and Φ_{J_2}, satisfy

$$\Phi_{J_1} + \Phi_{J_2} = \Phi. \tag{2.32}$$

Circuit diagram of the device is drawn in Fig. 2.5. Instead of deriving the Lagrangian for

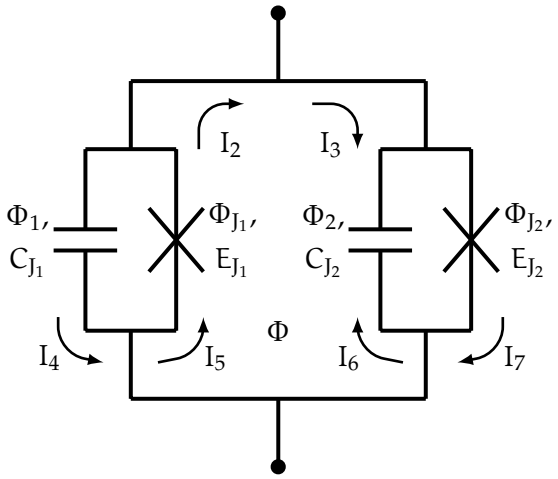

Figure 2.5: **dc SQUID equivalent circuit**. The cross symbol represents the inductive part of a Josephson junction. The total flux through the loop, away from the viewer, is labeled by Φ. Capitalized symbols represent the branch variables, and non-capital symbols the node variables. Arrows indicate the convention for the positive direction of current.

the device, we are content in showing that the dc SQUID works similarly to a CPB. The currents through the junctions are given by the Josephson relation Eq. (2.24), as

$$\begin{aligned} I_5 &= I_{c_1} \sin\left(2\pi \frac{\Phi_{J_1}}{\Phi_0}\right), \\ I_7 &= I_{c_2} \sin\left(2\pi \frac{\Phi_{J_2}}{\Phi_0}\right). \end{aligned}$$

According to Kirchhoff's current law (Eq. (2.8)), the net current through the SQUID is given by

$$\begin{aligned} I_{net} &= I_2 - I_3 \\ &= \tilde{I}_c \left[\sin\left(2\pi \frac{\Phi_{J_1}}{\Phi_0}\right) - \sin\left(2\pi \frac{\Phi_{J_2}}{\Phi_0}\right)\right], \end{aligned}$$

where the last equality holds for a symmetric SQUID, for which $I_{c_1} = I_{c_2} := \tilde{I}_c$. Rewriting $\Phi_{J_1} = [\Phi - (\Phi_{J_2} - \Phi_{J_1})]/2$ (Eq. (2.32)) and $\Phi_{J_2} = [\Phi + (\Phi_{J_2} - \Phi_{J_1})]/2$, with the help of

trigonometric identities

$$\begin{aligned} I_{net} &= \tilde{I}_c \left[\sin\left(\pi \frac{\Phi - (\Phi_{J_2} - \Phi_{J_1})}{\Phi_0}\right) + \sin\left(\pi \frac{\Phi + (\Phi_{J_2} - \Phi_{J_1})}{\Phi_0}\right) \right] \\ &= \tilde{I}_c \left[\sin\left(\pi \frac{\Phi_{J_2} - \Phi_{J_1}}{\Phi_0}\right) \cos\left(\pi \frac{\Phi}{\Phi_0}\right) - \cos\left(\pi \frac{\Phi_{J_2} - \Phi_{J_1}}{\Phi_0}\right) \sin\left(\pi \frac{\Phi}{\Phi_0}\right) \right. \\ &\quad \left. + \sin\left(\pi \frac{\Phi_{J_2} - \Phi_{J_1}}{\Phi_0}\right) \cos\left(\pi \frac{\Phi}{\Phi_0}\right) + \cos\left(\pi \frac{\Phi_{J_2} - \Phi_{J_1}}{\Phi_0}\right) \sin\left(\pi \frac{\Phi}{\Phi_0}\right) \right] \\ &= 2\tilde{I}_c \cos\left(\pi \frac{\Phi}{\Phi_0}\right) \sin\left(\pi \frac{\Phi_{J_2} - \Phi_{J_1}}{\Phi_0}\right). \end{aligned} \tag{2.33}$$

For the variables

$$I_c := 2\tilde{I}_c \cos\left(\pi \frac{\Phi}{\Phi_0}\right), \tag{2.34}$$

$$\Phi_J := \frac{\Phi_{J_2} - \Phi_{J_1}}{2}, \tag{2.35}$$

Equation (2.33) is the Josephson relation of Eq. (2.24), which means that the inductive energy over the SQUID is of the form of Eq. (2.27). Assuming that the geometric inductance, and thus the magnetic energy of the SQUID loop is negligible [35], the capacitive energy of the SQUID is given by

$$\begin{aligned} T_{J_1} + T_{J_2} &= C_{J_1} \frac{\dot{\Phi}_{J_1}^2}{2} + C_{J_2} \frac{\dot{\Phi}_{J_2}^2}{2} \\ &= \left(C_{J_1} + C_{J_2}\right) \frac{\dot{\Phi}_J^2}{2}. \end{aligned}$$

Thus, the Lagrangian of the voltage-biased dc SQUID is given by Eq. (2.29), with Φ-dependent I_c.

2.2.5 Transmission-line-shunted plasma oscillation qubit

In a transmon, a dc SQUID is capacitively coupled to a CPW resonator, which is excited with microwaves. The SQUID is used as the qubit. A cartoon of the device, originally considered by Koch et al. in [33], is shown in Fig. 2.6. The device may be modelled with the circuit shown in Fig. 2.7 [33]. Here, the CPW-resonator is modelled as an LC-oscillator, as is motivated in Sec. 2.2.2. As was shown in Sec. 2.2.4, the SQUID-loop can be modelled as a single Josephson junction with a tunable Josephson energy, with effective flux Φ_J given by Eq. (2.35), tunable Josephson energy given by Eq. (2.34), and an effective capacitance, C_{eff}, which accounts for capacitances from both junctions.

Choosing the branches with coordinate variables Φ_{J_C}, Φ_{r_C}, Φ_g and Φ_p as closure branches leaves Φ_J, Φ_r and Φ_b in the spanning tree. Kirchhoff's voltage law (Eq. (2.9))

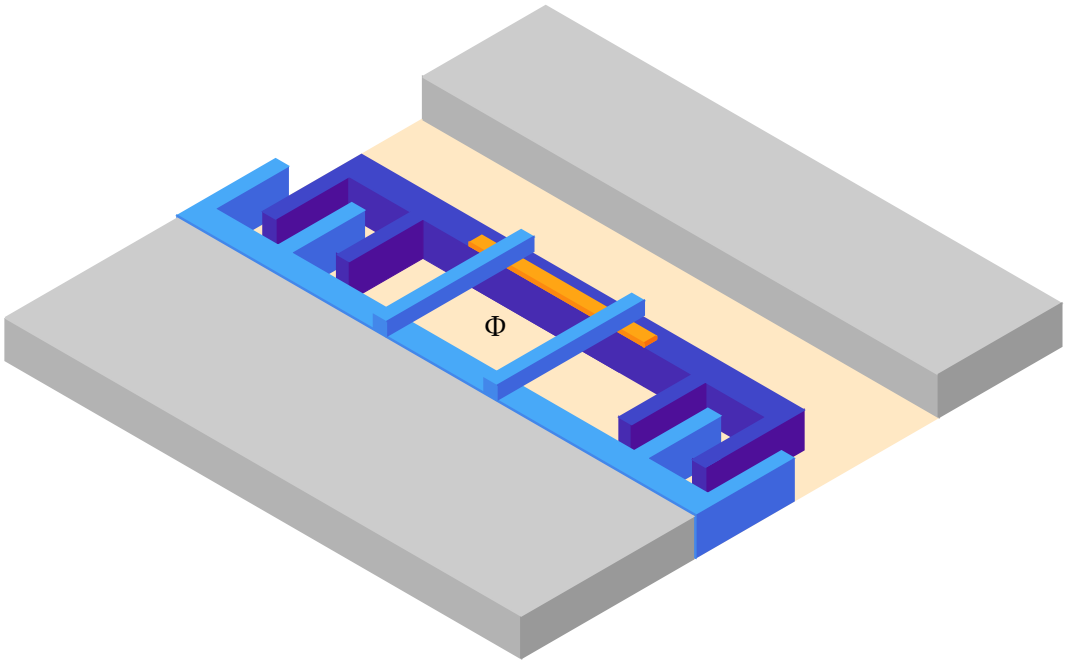

Figure 2.6: **SQUID embedded in a transmission-line resonator.** Part of ground (wide gray block) and the center conductor (narrow gray block) of a long transmission-line. Two superconducting islands (blue blocks) separated by a non-superconducting barrier (orange, thin block) lay between the transmission-line conductors. The reservoir (light blue) is shunted to ground, while the island (dark blue) is not. Picture is not to scale.

relates the closure branch variables to the spanning branch variables, as

$$\begin{aligned}\Phi_{r_C} &= -\Phi_r,\\ \Phi_{J_C} &= -\Phi_J,\\ \Phi_p &= -\Phi_r - \Phi_b,\\ \Phi_g &= \Phi_r - \Phi_J.\end{aligned}$$

The transmon contains four nodes: ground, input port, resonator and the island. Taking the voltage source as a large-capacitance capacitor, renders the input port node as passive, leaving ϕ_r and ϕ_J as the dynamical degrees of freedom. We ignore the capacitive energy of the voltage source as an unobservable constant. The definition (2.10) relates the spanning branch variables to the node variables, as

$$\begin{aligned}\Phi_r &= \phi_{gnd} - \phi_r,\\ \Phi_J &= \phi_{gnd} - \phi_J,\\ \Phi_b &= \phi_p - \phi_{gnd}.\end{aligned}$$

We take $\phi_{gnd} = 0$. Using the result of Eq. (2.17) for the energy of a capacitor, the capacitive

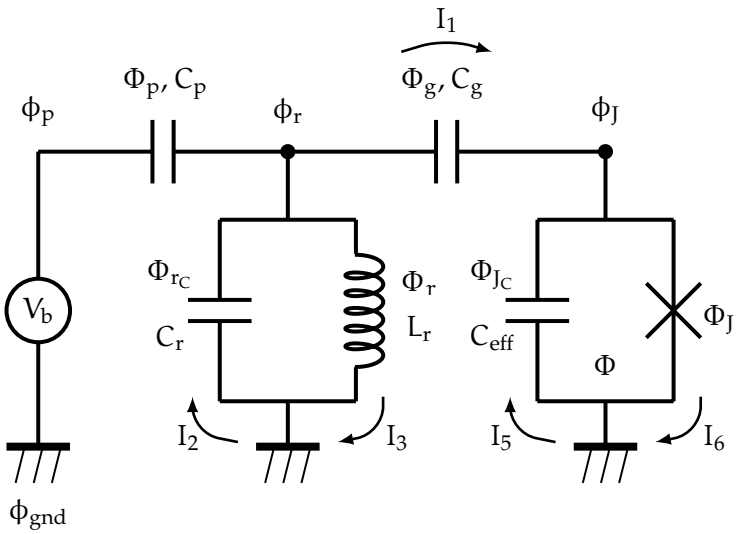

Figure 2.7: **Transmon equivalent circuit**. Cross symbol represents the nonlinear inductor related to a Josephson junction. Capital Φ-symbols label the branch variables, while non-capitalised ϕ-symbols are reserved for the node variables. Bold circles are drawn for each active node, and arrows for directions of currents.

energy terms of the transmon are

$$\begin{aligned} T_p &= C_p \frac{\dot{\Phi}_p^2}{2} = C_p \frac{(\dot{\phi}_r - C_p V_b)^2}{2} \\ T_{r_C} &= C_r \frac{\dot{\Phi}_r^2}{2} = C_r \frac{\dot{\phi}_r^2}{2}, \\ T_g &= C_g \frac{\dot{\Phi}_g^2}{2} = C_g \frac{(\dot{\phi}_J - \dot{\phi}_r)^2}{2}, \\ T_{J_C} &= C_{eff} \frac{\dot{\Phi}_{J_C}^2}{2} = C_{eff} \frac{\dot{\phi}_J^2}{2}. \end{aligned}$$

There are two inductive energy terms, given by Eqs. (2.18) and (2.27), as

$$\begin{aligned} U_r &= \frac{\phi_r^2}{2L_r}, \\ U_J &= -E_J(\Phi) \cos\left(2\pi \frac{\phi_J}{\Phi_0}\right). \end{aligned}$$

Thus, the Lagrangian is given by

$$\begin{aligned} L &= \sum_i T_i - \sum_j U_j \\ &= (C_p + C_r + C_g)\frac{\dot{\phi}_r^2}{2} - \frac{\phi_r^2}{2L_r} + (C_g + C_{eff})\frac{\dot{\phi}_J^2}{2} - C_g \dot{\phi}_J \dot{\phi}_r + E_J(\Phi)\cos\left(2\pi\frac{\phi_J}{\Phi_0}\right) - C_p V_b \dot{\phi}_r + C_p \frac{V_b^2}{2}. \end{aligned}$$

The associated conjugate variables are calculated, as

$$q_r = \frac{\partial L}{\partial \dot{\phi}_r} = \left(C_p + C_g + C_r\right)\dot{\phi}_r + V_b C_p - C_g \dot{\phi}_J, \tag{2.36}$$

$$q_J = \frac{\partial L}{\partial \dot{\phi}_J} = \left(C_g + C_{eff}\right)\dot{\phi}_J - C_p \dot{\phi}_r. \tag{2.37}$$

As a consequence, the Hamiltonian assumes the form

$$\begin{aligned} H &= q_r\dot{\phi}_r + q_J\dot{\phi}_J - L \\ &= (C_p{+}C_r{+}C_g)\frac{\dot{\phi}_r^2}{2} + \frac{\phi_r^2}{2L_r} + (C_g{+}C_{eff})\frac{\dot{\phi}_J^2}{2} - C_g\dot{\phi}_J\dot{\phi}_r - E_J(\Phi)\cos\left(2\pi\frac{\phi_J}{\Phi_0}\right) - C_p\frac{V_b^2}{2}. \end{aligned} \tag{2.38}$$

By solving Eqs. (2.36) and (2.37) for $\dot{\phi}_r$ and $\dot{\phi}_J$, the Hamiltonian may be written as a function of the conjugate charges, as

$$\begin{aligned} H =& \frac{C_g + C_{eff}}{2C_*^2}q_r^2 + \frac{\phi_r^2}{2L_r} \\ &+ \frac{C_p + C_g + C_r}{2C_*^2}q_J^2 - E_J(\Phi)\cos\left(2\pi\frac{\phi_J}{\Phi_0}\right) \\ &+ \frac{C_g}{C_*^2}q_J q_r + \frac{V_b C_p C_g}{C_*^2}q_J + \frac{V_b C_p\left(C_g + C_{eff}\right)}{C_*^2}q_r - \frac{C_p\left[C_*^2 - C_p(C_g + C_{eff})\right]V_b^2}{2C_*^2}, \end{aligned}$$

where $C_*^2 = (C_p + C_g + C_r)C_{eff} + (C_p + C_r)C_g$. In the limit $C_r \gg C_{eff}, C_p, C_g$,

$$\begin{aligned} C_*^2 &\to C_r(C_g + C_{eff}), \\ q_r &\to C_r\dot{\phi}_r, \end{aligned}$$

which simplify the Hamiltonian to

$$\begin{aligned} H =& \frac{q_r^2}{2C_r} + \frac{\phi_r^2}{2L_r} \\ &+ \frac{q_J^2}{2(C_g + C_{eff})} - E_J(\Phi)\cos\left(2\pi\frac{\phi_J}{\Phi_0}\right) \\ &+ \frac{C_g}{(C_g + C_{eff})C_r}q_r q_J + \frac{C_p}{C_r}V_b q_r - C_p\frac{V_b^2}{2} + \mathcal{O}(C/C_r), \end{aligned}$$

where $C \in \{C_{eff}, C_g, C_p\}$. The first two terms describe the energy of a free LC oscillator. The following two terms account for the SQUID energy, and the energy of the free SQUID. The term $C_p V_b^2/2$ does not affect the equations of motion, and may be dropped. The term proportional to $q_J q_r$ constitutes the SQUID-oscillator interaction. The remaining term $\propto V_b q_r$ causes an offset to the resonator charge. It can be absorbed into the

kinetic term of the oscillator, as

$$\frac{q_r^2}{2C_r} + \frac{C_p}{C_r} V_b q_r + \mathcal{O}(C_p^2/C_r) = \frac{(q_r + C_p V_b)^2}{2C_r} + \mathcal{O}(C_p^2/C_r),$$

Furthermore, by defining $q_{r,\mathrm{eff}} = q_r + C_p V_b$, the interaction term can be rewritten, as

$$\frac{C_g}{(C_g + C_{\mathrm{eff}})C_r}(q_{r,\mathrm{eff}} - C_p V_b) q_J = \frac{C_g}{(C_g + C_{\mathrm{eff}})C_r} q_{r,\mathrm{eff}} q_J - \frac{C_g C_p}{(C_g + C_{\mathrm{eff}})C_r} V_b q_J.$$

The last term may be absorbed into the SQUID degrees of freedom, as

$$\frac{q_J^2}{2(C_g + C_{\mathrm{eff}})} - \frac{C_g C_p}{(C_g + C_{\mathrm{eff}})C_r} V_b q_J + \mathcal{O}(C_g C_p/C_r) = \frac{(q_J - C_g C_p C_r^{-1} V_b)^2}{2(C_g + C_{\mathrm{eff}})} + \mathcal{O}(C_g C_p/C_r).$$

We quantize the degrees of freedom, as

$$\begin{aligned} \phi_r &\to \hat{\phi}_r \otimes \hat{\mathbf{I}}_{\mathrm{SQUID}}, \\ q_{r,\mathrm{eff}} &\to \hat{q}_{r,\mathrm{eff}} \otimes \hat{\mathbf{I}}_{\mathrm{SQUID}}, \\ \phi_J &\to \hat{\mathbf{I}}_r \otimes \hat{\phi}_J, \\ q_J &\to \hat{\mathbf{I}}_r \otimes \hat{q}_J, \end{aligned}$$

with the canonical commutation relations

$$\begin{aligned} [\hat{\phi}_r, \hat{q}_{r,\mathrm{eff}}] &= i\hbar \\ [\hat{\phi}_J, \hat{q}_J] &= i\hbar. \end{aligned}$$

The tensor products between the subsystems will not be written explicitly henceforth. In terms of the ladder operators (Eqs. (2.21) and (2.22)), the LC oscillator energy may be written in the form of Eq. (2.23). Likewise, with $\hat{n} = \hat{q}_J/(2e)$ and $n_g = C_g C_p V_b/(2eC_r)$, the SQUID energy assumes the form of Eq. (2.29). The voltage operator defined by the relation $\hat{q}_{r,\mathrm{eff}} = C_r \hat{V}_r$, expressed in terms of the oscillator ladder operators, is given by $\hat{V}_r = V_{0,\mathrm{rms}}(\hat{a} + \hat{a}^\dagger)$, where $V_{0,\mathrm{rms}} = \sqrt{\hbar\omega_r/(2C_r)}$ [33]. Finally, we arrive at the quantum Hamiltonian for the transmon,

$$\hat{H} = \hbar\omega_r \hat{a}^\dagger \hat{a} + 4E_C \hat{n}^2 - E_J(\Phi)\cos(\hat{\varphi}) + \frac{2C_g V_{0,\mathrm{rms}}}{C_{\mathrm{eff}} + C_g}(\hat{a} + \hat{a}^\dagger)\hat{n}. \tag{2.39}$$

The transmon is operated in the regime $E_J \gg E_C$ to reduce charge dispersion, that is, the dependence of the SQUID energy levels on the offset charge (see Fig. 2.8). While the n_g-dependence decreases exponentially, $E_m(n_g = 1/2) - E_m(n_g = 0) \propto e^{-\sqrt{E_J/E_C}}$, as a function of E_J/E_C, the anharmonicity also decreases, but only by a power law, $\alpha \propto (E_J/E_C)^{-a}$, where a is a constant [33]. Thus it is possible to diminish n_g dependence while retaining sufficient anharmonicity to be able to operate the SQUID as a two-level

system.

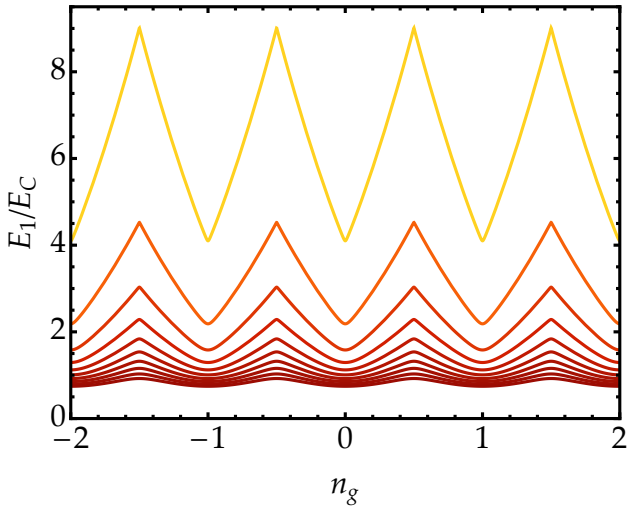

Figure 2.8: **Offset charge dependence of CPB energy levels.** The eigenenergy to charging-energy ratio E_1/E_C (Eq. (2.31)) as a function of the offset charge n_g. Darker color indicates a higher E_J/E_C ratio. Plotted ratios are $E_J/E_C = 1/i$, $i \in \{1, ..., 10\}$.

Chapter 3

Physics with transmons

3.1 Transmon perturbation theory

In [33], the qubit is compared to a charged, massive quantum rotor in a homogeneous gravitational field[1], which pulls the mass towards $\varphi = 0$. The rotor is simultaneously in a magnetic field[2], which drives the charged mass to rotate. In the limit $E_J/E_C \gg 1$, the gravitational field dominates the dynamics, keeping the angle of rotation small. This is taken as the motivation for the perturbative approach around $\varphi = 0$, where the CPB Hamiltonian (Eq. (2.29)) is expanded, as

$$\hat{H} \approx 4E_C(\hat{n} - n_g)^2 - E_J\left(1 - \frac{1}{2!}\hat{\varphi}^2 + \frac{1}{4!}\hat{\varphi}^4\right). \tag{3.1}$$

In this picture, the periodicity of φ is lost, which leads to a lack of description of charge dispersion, as it becomes possible to gauge transform away the n_g-dependence. As discussed in Sec. 2.2.5, this is not an assumption, but instead is consistent with taking $E_J/E_C \gg 1$. Without n_g-dependence we recognise (3.1) as a quantum harmonic oscillator with $\hat{\varphi}^4$ perturbation. The ladder operators $\hat{a}^{(0)}$ and $\hat{a}^{\dagger(0)}$ of the associated harmonic oscillator assume the forms

$$\hat{a}^{(0)} = \left(\frac{E_J}{2^5 E_C}\right)^{1/4}\left(\hat{\varphi} + i\sqrt{\frac{8E_C}{E_J}}\hat{n}\right),$$
$$\hat{a}^{\dagger(0)} = \left(\frac{E_J}{2^5 E_C}\right)^{1/4}\left(\hat{\varphi} - i\sqrt{\frac{8E_C}{E_J}}\hat{n}\right),$$

such that

$$\hat{H} = \sqrt{8E_C E_J}\left(\hat{a}^{\dagger(0)}\hat{a}^{(0)} + \frac{1}{2}\right) - E_J - \frac{E_C}{12}\left(\hat{a}^{\dagger(0)} + \hat{a}^{(0)}\right)^4.$$

[1] the potential term proportional to the Josephson energy
[2] terms proportional to n_g

The perturbative expansion with

$$|m\rangle \approx |m^{(0)}\rangle + \left(\frac{E_C}{E_J}\right)|m^{(1)}\rangle = |m^{(0)}\rangle - \frac{E_C}{12}\sum_{k,k\neq m}\frac{\langle k^{(0)}|\left(\hat{a}^{\dagger(0)}+\hat{a}^{(0)}\right)^4|m^{(0)}\rangle}{E_k^{(0)}-E_m^{(0)}}|m^{(0)}\rangle, \tag{3.2}$$

$$E_m \approx E_m^{(0)} + \left(\frac{E_C}{E_J}\right)E_m^{(1)} = \sqrt{8E_CE_J}\left(m+\frac{1}{2}\right) - \frac{E_C}{12}\langle m^{(0)}|\left(\hat{a}^{\dagger(0)}+\hat{a}^{(0)}\right)^4|m^{(0)}\rangle, \tag{3.3}$$

then yields the eigenvalues

$$E_m = \sqrt{8E_CE_J}\left(m+\frac{1}{2}\right) - E_J - \frac{E_C}{12}\left(6m^2+6m+3\right), \tag{3.4}$$

where m runs from 0 to infinity. Thus, the transition energy between the ground and the first excited state is given by

$$E_{1,0} = E_1 - E_0 = \sqrt{8E_CE_J} - E_C. \tag{3.5}$$

For $E_J = E_{J,max}$, the transition frequency $E_{1,0}/\hbar$ is also known as the plasma oscillation frequency. Since the eigenstates, by definition, diagonalize the Hamiltonian, the transmon Hamiltonian (Eq. (2.39)) can be expressed as

$$\hat{H} = \hbar\omega_r\hat{a}^\dagger\hat{a} + \hbar\sum_{m=0}^{\infty}\omega_m|m\rangle\langle m| + \hbar\sum_{m,k}g_{m,k}\left(\hat{a}^\dagger+\hat{a}\right)|m\rangle\langle k|, \tag{3.6}$$

where $\hbar\omega_m = E_m$, and the *coupling constant* between states m and k is defined as

$$g_{m,k} = \frac{2C_geV_{0,rms}}{C_{eff}+C_g}\langle m|\hat{n}|k\rangle, \tag{3.7}$$

which are hermitian, i.e. $g_{m,k} = g_{k,m}^*$. For large E_J/E_C ratio the system is dominated by the harmonic oscillator, and the number operator is just

$$\hat{n} = \frac{1}{\sqrt{2}}\left(\frac{E_J}{8E_C}\right)^{1/4}\left(\hat{a}^{(0)}-\hat{a}^{\dagger(0)}\right).$$

Likewise, when $E_J/E_C \to \infty$, the matrix element

$$\begin{aligned}\langle k|\hat{n}|m\rangle &\to \frac{1}{\sqrt{2}}\left(\frac{E_J}{8E_C}\right)^{1/4}\langle k^{(0)}|\left(\hat{a}^{(0)}-\hat{a}^{\dagger(0)}\right)|m^{(0)}\rangle \\ &= \begin{cases} -\sqrt{\frac{m+1}{2}}\left(\frac{E_J}{8E_C}\right)^{1/4}, & \text{when } k = m+1 \\ \sqrt{\frac{m}{2}}\left(\frac{E_J}{8E_C}\right)^{1/4}, & \text{when } k = m-1 \\ 0, & \text{when } k = m\pm l, l>1. \end{cases}\end{aligned}$$

From this we conclude that in the transmon regime, the qubit state i only significantly couples to the states $i \pm 1$. In the *rotating wave approximation*, where the terms that simultaneously excite or de-excite both the qubit and the resonator, are ignored, the transmon Hamiltonian (Eq. (3.6)) is given by

$$\hat{H} = \hbar\omega_r \hat{a}^\dagger \hat{a} + \hbar \sum_{m=0}^{\infty} \omega_m |m\rangle\langle m| + \hbar \sum_{m=0}^{\infty} \left(g_{m,m+1} \hat{a}^\dagger |m\rangle\langle m+1| + g_{m+1,m} \hat{a} |m+1\rangle\langle m| \right). \tag{3.8}$$

3.1.1 Dispersive limit

The dispersive limit, $\lambda_i := g_{i,i+1}/\mathrm{abs}(\omega_{i+1} - \omega_i - \omega_r) \ll 1$, in which the qubit-resonator detuning $\Delta_i = (\omega_{i+1} - \omega_i - \omega_r)$ is large, is usually treated by means of a so-called *canonical transformation*. This is a perturbative approach in that the Hamiltonian is of the form $\hat{H} = \hat{H}_0 + \sum_i \lambda_i(\Delta_i \hat{V}_i)$. Instead of calculating approximative eigenvalues and eigenvectors to the original Hamiltonian, a canonical transformation, $\hat{A} = \hat{I} + \sum_i \mathcal{O}(\lambda_i)$, $\hat{D}^\dagger = \hat{D}^{-1}$, transforms the Hamiltonian $\hat{H} \to \hat{H}' := \hat{D}\hat{H}\hat{D}^\dagger$, where $\hat{H}'$ is exactly solvable. Applying the transformation n times results in a Hamiltonian where the lowest-order interaction terms are of order $n+1$. Here the appropriate operators are given by [33],

$$\begin{aligned} \hat{D} &= e^{i(\hat{S} - \hat{S}^\dagger)}, \\ \hat{S} &= \sum_i \frac{g_{i,i+1}}{\omega_{i,i+1} - \omega_r} \hat{a} |i+1\rangle\langle i|, \end{aligned}$$

where we have introduced the short-hand $\omega_{i,i+1} = \omega_{i+1} - \omega_i$ for the transition frequency between qubit levels i and $i+1$. The resulting transformed Hamiltonian, up to order $g_{i,j}^2/(\omega_{i,i+1} - \omega_r)^2$ is given by [33]

$$\begin{aligned} \hat{H}' =& \hbar\omega_r \hat{a}^\dagger \hat{a} + \hbar \sum_{m=0}^{\infty} \omega_m |m\rangle\langle m| + \hbar \sum_{m=0}^{\infty} \chi_{m,m+1} |m+1\rangle\langle m+1| - \hbar\chi_{0,1} \hat{a}^\dagger \hat{a} |0\rangle\langle 0| \\ &+ \hbar \sum_{m=1}^{\infty} (\chi_{m-1,m} - \chi_{m,m+1})\, \hat{a}^\dagger \hat{a} |m\rangle\langle m| \\ &+ \hbar \sum_{m=0}^{\infty} \frac{g_{m,m+1} g_{m,m+2} \left[(\omega_{m+1} - \omega_{m+2}) - (\omega_m - \omega_{m+1}) \right]}{2(\omega_{m+1} - \omega_m - \omega_r)(\omega_{m+2} - \omega_{m+1} - \omega_r)} \hat{a}\hat{a} |m+2\rangle\langle m| + \text{h.c.} \end{aligned}$$

When two-photon transitions are ignored, and the qubit is approximated as a two-state system, the resulting dispersive Hamiltonian reduces to

$$\hat{H} = \frac{1}{2}\hbar\omega_q' \hat{\sigma}_z + (\hbar\omega_r' + \hbar\chi\hat{\sigma}_z) \hat{a}^\dagger \hat{a}, \tag{3.9}$$

where $\omega_q' = \omega_q + \chi_{01}$, and $\omega_r' = \omega_r - \chi_{12}/2$ are so-called renormalized frequencies, and $\omega_q = \omega_{1,0}$. The *partial dispersive shifts* are given by

$$\chi_{ij} = \frac{g_{i,j}^2}{(\omega_{i,j} - \omega_r)}. \tag{3.10}$$

The total dispersive shift is given by

$$\chi = \chi_{01} - \frac{\chi_{12}}{2}. \tag{3.11}$$

In the dispersive Hamiltonian (Eq. (3.9)), the qubit-resonator interaction is reduced to ac-Stark shifts in the resonator and qubit resonance frequencies. The qubit-state-dependent shift in resonator frequency is used for inferring the state of the qubit, enabling transmission- or reflection measurements through the resonator transmission line. In Ref. [36], the ac Stark shift is written, as

$$\omega_q' = \omega_q + \frac{g_{q,r}^2}{(\omega_q - \omega_r)} - \frac{2\overline{n} g_{q,r}^2}{(\omega_q - \omega_r)}, \tag{3.12}$$

where $g_{q,r} = g_{0,1}$, and the the second term in the sum is referred to as the Lamb shift, often not experimentally separable from the bare frequency. The last term corresponds to the ac Stark shift, and $\overline{n}$ is the average number of photons inside the resonator.

3.1.2 Rabi oscillation

Approximating the number basis $\{|m\rangle\}$ by $\{|g\rangle, |e\rangle\}$, which is valid as long as the available exchange energy with the photons is sufficiently small, the Hamiltonian of Eq. (3.8) reduces to the *Jaynes-Cummings Hamiltonian*,

$$\hat{H} = \hbar\omega_q \hat{\sigma}_z + \hbar\omega_r(\hat{a}^\dagger \hat{a} + 1/2) + \hbar g_{q,r}\left(\hat{a}^\dagger |g\rangle\langle e| + \hat{a}|e\rangle\langle g|\right). \tag{3.13}$$

We have also employed the rotating-wave approximation. The eigenstates and eigenvalues for n photons are given by [37]

$$\begin{aligned} E_{\pm,n} &= \hbar\omega_r(n + 1/2) \pm \Omega_n, \\ |+, n\rangle &= \sin(\Phi_n/2)|g\rangle|n+1\rangle + \cos(\Phi_n/2)|e\rangle|n\rangle, \\ |-, n\rangle &= \cos(\Phi_n/2)|g\rangle|n+1\rangle - \sin(\Phi_n/2)|e\rangle|n\rangle, \end{aligned}$$

where $\sin(\Phi_n/2) = \sqrt{(\Omega_n - \Delta)/(2\Omega_n)}$, $\cos(\Phi_n/2) = \sqrt{(\Omega_n + \Delta)/(2\Omega_n)}$, the detuning $\Delta = \Delta_0$, and $\Omega_n = \sqrt{\Delta^2 + 4g_{q,r}^2(n+1)}$. For zero detuning Ω_n is known as the *Rabi frequency*. The qubit-resonator interaction causes he qubit population to oscillate between

the ground and excited states, which may be observed from the probability

$$\begin{aligned} P(e|g) &= |\langle e|U(t,t_0)|g\rangle|^2 \\ &= \left|\langle e|\left[2\sin(\Phi_n/2)|+,n\rangle e^{-iE_+t/\hbar} + 2\cos(\Phi_n/2)|-,n\rangle e^{-iE_-t/\hbar}\right]\right|^2 \\ &= -\frac{1}{4}\left[-2+2\cos(2tg_{q,r}\sqrt{n+1})\right]4\sin^2(\Phi_n/2) \\ &= \sin^2\left(tg_{q,r}\sqrt{n+1}\right), \end{aligned}$$

where we have taken qubit state at zero time to be the ground state, for concreteness.

3.1.3 Coupling constants

The strength of the qubit-resonator interaction is measurable when the two subsystems are at so-called *avoided crossing*. For a simple two-state system described by the Rabi Hamiltonian

$$\hat{H} = E_1|1\rangle\langle 1| + E_2|2\rangle\langle 2| + \hbar g|1\rangle\langle 2| + \hbar g^*|2\rangle\langle 1|, \tag{3.14}$$

the coupling constant g perturbs the bare states $|1\rangle$ and $|2\rangle$, leading to the energy eigenvalues

$$E_\pm = \frac{1}{2}(E_1+E_2) \pm \frac{1}{2}\sqrt{(E_1-E_2)^2+4g^2}, \tag{3.15}$$

also referred to as dressed energies. As a function of either bare energy, the dressed energies with nonzero coupling never become degenerate, and instead smoothly avoid the cross-over, as indicated by Fig. 3.1 (b). The shortest distance between the eigenenergies, at $\partial_{E_1}(E_+ - E_-) = 0$, i.e. at $E_1 = E_2$, is $2g$. Thus, spectroscopic observation of an avoided crossing provides a way to measure the coupling constant.

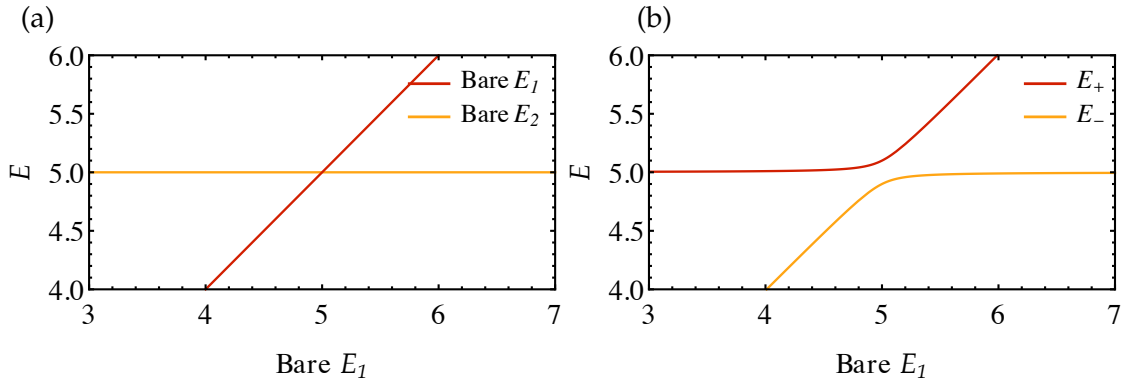

Figure 3.1: **Avoided crossing as a function of bare energy**. (a) The Rabi model bare energies, which are the eigenvalues of the noninteracting two-state system (Eq. (3.14)). (b) The Rabi model dressed energies (Eq. (3.15)), with $g = 0.1$.

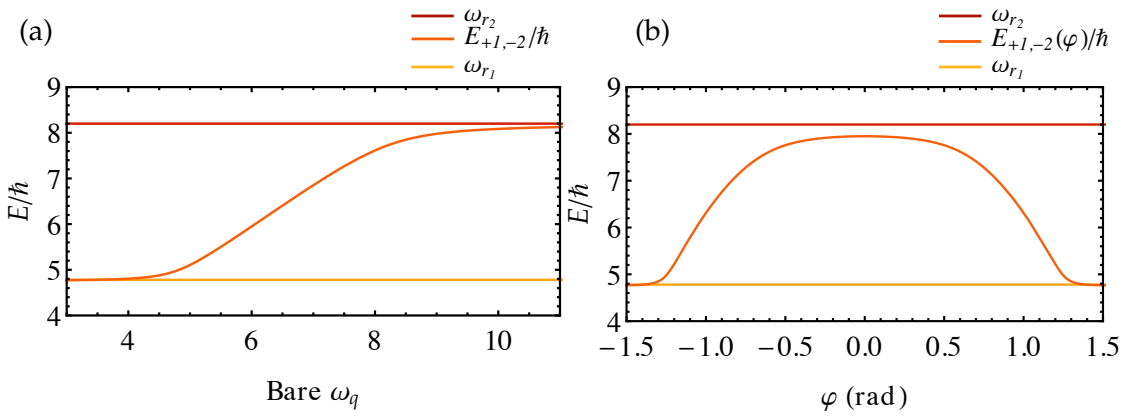

Figure 3.2: **Avoided crossing as a function of bare energy**. (a) The intermediate dressed energy in a system of one qubit and two resonators, as a function of the bare qubit frequency. (b) The intermediate dressed energy as a function of the phase.

In cQED, the tuning of the qubit bare energy states, or in practice, the bare transition frequency[3] ω_q, is realized by varying the external flux, which changes the phase, φ, of the Josephson energy of the qubit (Eq. (2.33)). For each resonator coupled to the qubit, there is an avoided crossing with the states $|e,0\rangle$ and $|g,1\rangle$, asserting that $\omega_{q,max}$ is not much smaller than the bare resonator frequency ω_r. Although it is possible to numerically solve for the dressed energies of the qubit–resonator system, obtained as solutions to the Jaynes Cummings type Hamiltonian (Eq. (3.13)), the eigenvalues are well approximated by analytic functions.

Let $\hat{H}$ be the Hamiltonian

$$\hat{H} = \hat{H}_0(x) + \hat{H}_1(x) + ... + \hat{H}_n(x), \tag{3.16}$$

where $\hat{H}_k(x)$, $k > 0$, are interaction terms between the subsystems, bare energies of which are given by the Hamiltonian $\hat{H}_0(x)$, and x is a continuous parameter. We assume that $x_1 < x_2 < ... < x_n$ are points such that $\hat{H}_k(x)$ dominates over other interaction terms at $x = x_k$. If the eigenvalues $E_{k,m}(x)$ to the Hamiltonian

$$\hat{H} = \hat{H}_0(x) + \hat{H}_k(x)$$

are known for each k, we propose that the eigenvalues of Eq. (3.16) may be approximated by continuous functions $E_m(x)$ which reduce to the numbers $E_{k,m}(x)$ at the limit $\hat{H}_i(x) \to 0, \forall i \neq k$. A Jaynes-Cummings Hamiltonian (Eq. (3.13)) for one qubit and two resonators

[3]Note that the transition energy and first excited state energy are used interchangeably, as the ground state energy is not observable.

reads

$$\begin{aligned}\hat{H} =&\hbar\omega_q\hat{\sigma}_z + \hbar\omega_{r_1}\hat{a}_1^\dagger\hat{a}_1 + \hbar\omega_{r_2}\hat{a}_2^\dagger\hat{a}_2 + \left(\hbar g_{q,r_1}\hat{a}_1^\dagger|g\rangle\langle e| + \text{h.c.}\right) + \left(\hbar g_{q,r_2}\hat{a}_2^\dagger|g\rangle\langle e| + \text{h.c.}\right) \\ :=&\hat{H}_{q,0} + \hat{H}_{r_1,0} + \hat{H}_{r_2,0} + \hat{H}_{q-r_1} + \hat{H}_{q-r_2},\end{aligned} \tag{3.17}$$

where subscripts 1 and 2 refer to the two resonators. In the region $[g_{q,r_2}/(\omega_q - \omega_{r_2})] \ll 1$, the interaction Hamiltonian $\hat{H}_{q-r_1}$ dominates over $\hat{H}_{q-r_2}$. Likewise, $\hat{H}_{q-r_2}$ dominates in the region $\text{abs}[g_{q,r_1}/(\omega_q - \omega_{r_1})] \ll 1$. Transforming the Hamiltonian of Eq. (3.17) in the subspace[4] $\{|e,0,0\rangle, |g,1,0\rangle, |g,0,1\rangle\}$ with the canonical transformation $\hat{D}_k = \exp(\hat{S}_k - \hat{S}_k^\dagger)$, $k = 1,2$, defined by

$$\begin{aligned}\hat{S}_1 &= \text{abs}\left(\frac{g_{q,r_1}}{\omega_q - \omega_{r_1}}\right)|e,0,0\rangle\langle g,1,0|, \\ \hat{S}_2 &= \text{abs}\left(\frac{g_{q,r_2}}{\omega_q - \omega_{r_2}}\right)|e,0,0\rangle\langle g,0,1|,\end{aligned}$$

yields the effective two-state systems

$$\begin{aligned}\hat{D}_1\hat{H}\hat{D}_1^\dagger =&\hbar\omega_q'|e,0,0\rangle\langle e,0,0| + \hbar\omega_{r_1}'|g,1,0\rangle\langle g,1,0| \\ &+\hbar\omega_{r_2}|g,0,1\rangle\langle g,0,1| + \left(\hbar g_{q,r_1}|g,1,0\rangle\langle e,0,0| + \text{h.c.}\right), \\ \hat{D}_2\hat{H}\hat{D}_2^\dagger =&\hbar\omega_q'|e,0,0\rangle\langle e,0,0| + \hbar\omega_{r_2}'|g,0,1\rangle\langle g,0,1| \\ &+\hbar\omega_{r_1}|g,1,0\rangle\langle g,1,0| + \left(\hbar g_{q,r_2}|g,0,1\rangle\langle e,0,0| + \text{h.c.}\right),\end{aligned}$$

where $\omega_q' = \omega_q + \text{abs}\left[g_{q,r_k}^2/(\omega_q - \omega_{r_k})\right]$ and $\omega_{r_k}' = \omega_{r_k} - \text{abs}\left[g_{q,r_k}^2/[\omega_q - \omega_{r_k})]\right\}$, $k = 1,2$, and terms of order $\mathcal{O}\left\{\text{abs}[g_{q,r_k}/(\omega_q - \omega_{r_k})]\right\}$ have been dropped out. Thus, for a transmon with $\omega_{r_1} \ll \omega_{r_2}$, in the region $\omega_q < \omega_{r_1}$ and up to order $\mathcal{O}\left\{\text{abs}[g_{q,r_k}^2/(\omega_q - \omega_{r_k})]\right\}$ the dressed energy of the system is approximately given by

$$E_-(\omega_q, \omega_{r_1}, g_{q,r_1}) = \frac{1}{2}\hbar\left(\omega_q + \omega_{r_1}\right) + \frac{1}{2}\sqrt{(\omega_q - \omega_{r_1})^2 + 4g_{q,r_1}^2} \tag{3.18}$$

of Eq. (3.15). Likewise, in the region $\omega_q > \omega_{r_2}$, the dressed energy is approximated by

$$E_+(\omega_q, \omega_{r_2}, g_{q,r_2}) = \frac{1}{2}\hbar\left(\omega_q + \omega_{r_2}\right) - \frac{1}{2}\sqrt{(\omega_q - \omega_{r_2})^2 + 4g_{q,r_2}^2}. \tag{3.19}$$

In the region $\omega_{r_1} < \omega_q < \omega_{r_2}$, we require the intermediate energy, denoted by $E_{+,-}$, to

[4] Apart from higher order many-photon transitions, suppressed by a factor of g_{q,r_k}^a, where a is the order of the transition, the dynamics are roughly described by the lowest available states for as long as the available energy, determined by the experimental setup, is limited.

be continuous and to satisfy

$$\lim_{g_{q,r_2}\to 0} E_{+_1,-_2} = E_+(\omega_q, \omega_{r_1}, g_{q,r_1}),\ \omega_q < \omega_{r_2},$$
$$\lim_{g_{q,r_1}\to 0} E_{+_1,-_2} = E_-(\omega_q, \omega_{r_2}, g_{q,r_2}),\ \omega_q > \omega_{r_1}.$$

Such a function is given by

$$E_{+_1,-_2}(\omega_q) = \frac{1}{2}\left[E_+(\omega_q, \omega_{r_1}, g_{q,r_1}) - E_-(\omega_q, \omega_{r_2}, g_{q,r_2})\right] + \frac{1}{2}\hbar\left(\omega_{r_1} + \omega_{r_2}\right). \tag{3.20}$$

Figure 3.3 compares the approximate eigenenergies of Eqs. (3.18), (3.19) and (3.20) with the eigenenergies obtained by numerically diagonalizing first the Cooper pair box Hamiltonian ((2.29)), and using the obtained solution in diagonalizing the associated Jaynes-Cummings type Hamiltonian for one qubit and two resonators (Eq. (3.17)). The CPB Hamiltonian was quantized in the number basis (see Appendix B), using 15 quanta. The Jaynes-Cummings type Hamiltonian was diagonalized in the resonator Fock space with 20 quanta, and in the $\{|g\rangle, |e\rangle\}$ subspace of the qubit. The approximate eigenvalues are in good agreement with the simulation and as such, are used for extracting the spectroscopic fitting parameters.

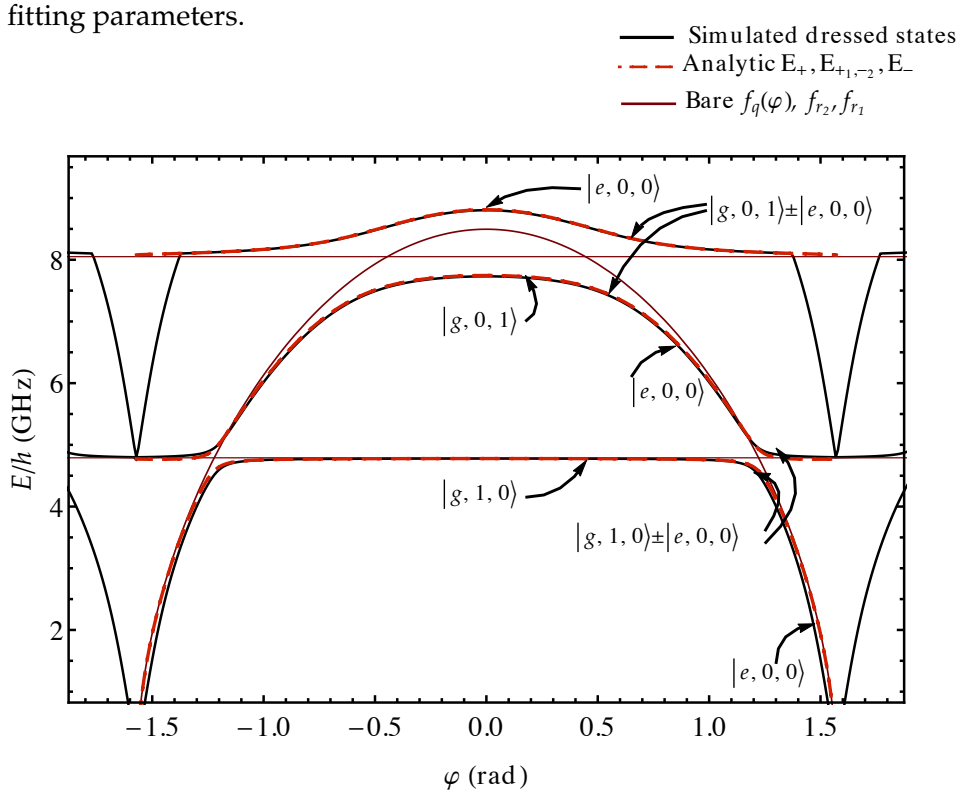

Figure 3.3: **Eigenvalues of the qubit-two-resonator system**. Energies corresponding to the lowest eigenstates, obtained by a numerical diagonalization of the Hamiltonian of Eq. (3.17) (black lines), as a function of the phase φ. Principle components of the eigenstates at various φ are indicated with arrows. The corresponding, approximate eigenenergies (Eqs. (3.18), (3.19) and (3.20)) (thick, red, dashed curves). For comparison, bare transition frequencies of the qubit and the two resonators are represented with red lines.

3.2 Environmental coupling and lifetimes

The inclusion of the effects of dephasing and decay requires extension to the standard formalism of quantum mechanics. While the time-evolution of a density operator of a closed system obeys the so-called von Neumann equation, the density operator of an open system obeys the so-called master equation of Lindblad form

$$\dot{\hat{\rho}} = -\frac{i}{\hbar}[\hat{H}, \hat{\rho}] + \sum_k \left[\hat{C}_k \hat{\rho} \hat{C}_k^\dagger - \frac{1}{2}(\hat{C}_k^\dagger \hat{C}_k \hat{\rho} + \hat{\rho} \hat{C}_k^\dagger \hat{C}_k)\right], \tag{3.21}$$

where $\hat{C}_k$ are Lindblad operators [38], $\hat{\rho}$ is the (reduced) density operator of the subsystem excluding the environmental degrees of freedom, and k runs over the relaxation and dephasing mechanisms. For a system with a qubit and a resonator, there are three Lindblad operators, $\hat{C}_1 = \sqrt{\gamma}|g\rangle\langle e|$, $\hat{C}_2 = \sqrt{\gamma_\phi}\hat{\sigma}_z$, and $\hat{C}_3 = \sqrt{\kappa}\hat{a}$, accounting for the relaxation and dephasing of the qubit, and the destruction of photons in the resonator. The Lindblad operators are phenomenological without additional knowledge of decay rates.

The inverses of the decay rates γ and γ_ϕ define the coherence times T_1 and T_ϕ. The *energy relaxation rate*, $\gamma = 1/T_1$ describes the rate at which the probability of finding the qubit in the first excited state falls. The *pure dephasing rate* $\gamma_\phi = 1/T_\phi$ describes the rate at which the absolute values of the off-diagonal density operator elements of the qubit fall. In other words, the time it takes for the phase difference between the logical states to randomize. They are related to the *ensemble-averaged decoherence time* T_2^*, which is obtained as the average over repeated measurements, as [39]

$$\frac{1}{T_2^*} = \frac{1}{2T_1} + \frac{1}{T_\phi}. \tag{3.22}$$

The time evolution consists of unitary driving pulses and free time-evolution, which rotate the qubit state on the Bloch sphere, as well as non-unitary evolution due to interaction with the noisy environment. Assuming free evolution after the initialization of the qubit to a pure state (Eq. (2.2)), it can be shown that the time-evolution given by Eq. (3.21), with Lindblad operators for T_1 and T_ϕ, cause exponential decay in the qubit density matrix elements, as [40]

$$\hat{\rho}(t) = (\rho_{00} + \rho_{11}e^{-t/T_1})|0\rangle\langle 0| + \rho_{11}e^{-t/T_1}|1\rangle\langle 1| + \rho_{01}e^{-t/T_\phi}|0\rangle\langle 1| + \rho_{01}^* e^{-t/T_\phi}|1\rangle\langle 0|. \tag{3.23}$$

As Rabi oscillation with $f_{drive} = f_q$ rotates the qubit Bloch vector about an axis in the xy-plane of the Bloch sphere, T_1 can be measured by performing a π-pulse, which rotates the Bloch vector by π, and waiting for a varying time before measurement [39]. So-called *Ramsey fringes* are produced with a sequence of two resonant $\pi/2$ pulses, between which there is a varying waiting time of t_{off} [39]. The first $\pi/2$ pulse ideally takes the qubit Bloch vector from the north pole on to the xy-plane. During t_{off}, there are no drive or probe

pulses so that the qubit undergoes free evolution, during which it precesses around the Bloch sphere at its excitation frequency. If $t_{off} = 0$, the second $\pi/2$ pulse along the same axis puts the qubit to the excited state. On the contrary, if $t_{off} = t_{\pi/2}$, the second $\pi/2$ pulse returns the qubit back to the ground state. While precessing, the state of the qubit decays according to Eq. (3.23). In an ensemble average, the effective decay constant is given by T_2^*. Thus, measurement of the qubit state in succession to application of a Ramsey pulse sequence provides a way to measure T_2^*.

3.3 Readout and spectroscopy

Microwave probe pulse of a given frequency is a coherent electromagnetic field. Interaction of the probe with a transmission-line resonator corresponds to a displacement of the vacuum state into a coherent state. Likewise, the qubit may be driven with a separate drive pulse. The interaction with the coherent field may be approximated as time-evolution under a time-dependent classical electromagnetic mode, [41], [38] as

$$\hat{H}_{q,drive} = \mathcal{E}\left(|e\rangle\langle g|e^{-i\omega t} + |g\rangle\langle e|e^{i\omega t}\right) = \mathcal{E}\left[\hat{\sigma}_x \cos(\omega t) + \hat{\sigma}_y \sin(\omega t)\right],$$

where $\mathcal{E}$ is the drive amplitude, and ω is the drive frequency. The Lorentzian lineshape of the qubit resonance can be derived from the so-called optical Bloch equation [42], [30]

$$\dot{\hat{\rho}} = -\frac{i}{\hbar}[\hat{H}, \hat{\rho}] - \frac{\gamma}{2}\left[|g\rangle\langle e|\hat{\rho}|e\rangle\langle g| - \frac{1}{2}\left(|e\rangle\langle e|\hat{\rho} + \hat{\rho}|e\rangle\langle e|\right)\right], \tag{3.24}$$

which is a master equation for the qubit degrees of freedom, including a simple model for qubit relaxation. Here, $\hat{H} = \hat{H}_0 + \hat{H}_{q,drive}$ with $H_0 = \hbar\omega_q/2\hat{\sigma}_z$. The so-called Bloch equations originally provided phenomenological models for spin-1/2 particles in magnetic fields [43]. The equations in Ref. [43] are written for the components of the magnetization vector, while in quantum optics, they are written for the components of the Bloch vector of the qubit (Eq. (2.4)).

Rotating into the frame of the drive field [44],

$$\begin{aligned}
\dot{\rho}' &:= \partial_t\left[e^{i\omega t\hat{\sigma}_z/2}\rho e^{-i\omega t\hat{\sigma}_z/2}\right] \\
&= i\frac{\omega t}{2}\hat{\sigma}_z e^{i\omega t\hat{\sigma}_z/2}\rho e^{-i\omega t\hat{\sigma}_z/2} + e^{i\omega t\hat{\sigma}_z/2}\left(\partial_t\rho\right)e^{-i\omega t\hat{\sigma}_z/2} - e^{i\omega t\hat{\sigma}_z/2}\rho e^{-i\omega t\hat{\sigma}_z/2} i\frac{\omega t}{2}\hat{\sigma}_z \\
&= e^{i\omega t\hat{\sigma}_z/2}\left(\partial_t\rho\right)e^{-i\omega t\hat{\sigma}_z/2} + \left[i\frac{\omega t}{2}\hat{\sigma}_z, \rho'\right],
\end{aligned}$$

the master equation for ρ' is equivalent with a master equation for ρ, with the Hamiltonian

$$\hat{H}' = e^{i\omega t\hat{\sigma}_z/2}\hat{H}e^{-i\omega t\hat{\sigma}_z/2} - \frac{\hbar\omega}{2}\hat{\sigma}_z.$$

Recalling that $\hat{\sigma}_a\hat{\sigma}_b = \delta_{ab}\mathbf{I} + i\varepsilon_{abc}\hat{\sigma}_c$, and that $\exp(i\omega t\hat{\sigma}_z) = \cos(\omega t)\mathbf{I} + i\sin(\omega t)\hat{\sigma}_z$, the first term is evaluated, as

$$
\begin{aligned}
&e^{i\omega t\hat{\sigma}_z/2}He^{-i\omega t\hat{\sigma}_z/2} \\
&= \hat{H}_0 + \cos(\omega t)\left[e^{i\omega t\hat{\sigma}_z/2}\hat{\sigma}_x e^{-i\omega t\hat{\sigma}_z/2}\right] + \sin(\omega t)\left[e^{i\omega t\hat{\sigma}_z/2}\hat{\sigma}_y e^{-i\omega t\hat{\sigma}_z/2}\right] \\
&= \hat{H}_0 + \mathcal{E}\cos(\omega t)\left\{\left[\cos^2\left(\frac{\omega t}{2}\right) - \sin^2\left(\frac{\omega t}{2}\right)\right]\hat{\sigma}_x - \sin(\omega t)\hat{\sigma}_y\right\} \\
&+ \mathcal{E}\sin(\omega t)\left[e^{i\omega t\hat{\sigma}_z/2}\hat{\sigma}_x e^{-i\omega t\hat{\sigma}_z/2}\right]i\hat{\sigma}_z \\
&= \hat{H}_0 + \mathcal{E}\cos(\omega t)\left[\cos(\omega t)\hat{\sigma}_x - \sin(\omega t)\hat{\sigma}_y\right] + \mathcal{E}\sin(\omega t)\left[\cos(\omega t)\hat{\sigma}_y + \sin(\omega t)\hat{\sigma}_x\right] \\
&= \hat{H}_0 + \mathcal{E}\hat{\sigma}_x.
\end{aligned}
$$

For H', Eq. (3.24) implies equations of motion for the density matrix elements, which are further expressed as equations of motion for the real-valued vector components n_x, n_y, and n_z (Eq. (2.4)), as

$$\dot{n}_x = \gamma n_x - 2(\omega - \omega_q)n_y, \tag{3.25}$$

$$\dot{n}_y = \frac{\gamma}{2}n_y - 2\mathcal{E}n_z + (\omega - \omega_q)n_x, \tag{3.26}$$

$$\dot{n}_z = -2\gamma\rho_{11} + 2\mathcal{E}n_y. \tag{3.27}$$

In a steady state [43], we take $\dot{n}_x = \dot{n}_y = \dot{n}_z = 0$. Comparing the density matrix elements (Eq. (2.2)) into those obtained with the Pauli decomposition (Eq. (2.3)), we observe that $\rho_{11} = (1 - n_z)/2$. Solving Eqs. (3.25), (3.26), and (3.27) for the Bloch vector components, and furthermore, for the excited state population yields a Lorentzian

$$\rho_{11} = \frac{1 - n_z}{2} = \frac{\mathcal{E}^2/2}{(\omega - \omega_q)^2 + 2\mathcal{E}^2 + \gamma^2/4}. \tag{3.28}$$

The photon population inside the resonator assumes a slightly more complicated lineshape due to the presence of a so-called Purcell filter, which is another transmission-line resonator capacitively coupled to the resonator (see Fig. 4.1 for an equivalent circuit). The Purcell filter operates as a band-pass filter, suppressing the decay of the qubit through the resonator. As will be discussed further in Chapter 4, measurements are performed by probing a microwave pulse through the resonator, and comparing the outgoing field with the incoming field. In terms of the transmission coefficient, $S_{21} = V_{out,2}/V_{in,1}$, the

lineshape of the resonance can be parameterized, as [45]

$$\mathrm{abs}\left[S_{21}(f_{probe})\right] = \mathrm{abs}\left\{\frac{A_0\ \kappa_{Pf}}{\left[\frac{1}{2}(\gamma_r+\kappa_{Pf})+i(f_{Pf}-f_{probe})+g_{r,Pf}^2/(\gamma_r/2-f_r+f_{probe})\right]}\right\}, \tag{3.29}$$

where A_0 is the amplitude, proportional to the input probe power, $g_{r,Pf}$ is the resonator–Purcell-filter coupling, κ_{Pf} is the decay rate of the Purcell filter, f_{probe} is the probe frequency, and γ_r is the internal loss rate of the resonators. The inverse of the decay rate is equal to the average time a photon remains in the transmission line. The internal loss rate is usually taken to be zero compared to the external loss rate. Reference [46] provides a theory of Purcell filters, and a more complete overview on their function.

Chapter 4

Experimental setup

4.1 Generation of control pulses

The state of the resonator is read out in homodyne detection of the transmission[1] coefficient through the resonator. As explained in Sec. 3.1.1, dispersive coupling between the qubit and the resonator causes a qubit-state-dependent shift in the resonance frequency of the resonator, which enables one to infer the state of the qubit in such a measurement scheme.

We employ separate control pulses for driving the qubit and for probing the resonator. The control pulses are generated by on-off modulation of analog microwave signal generators at room temperature. The generator SRS model SG396 is used to generate the probe pulse through the resonator. The generator Giga-tronics model 2550B is used to generate the driving pulses. These generators produce a continuous sinusoidal coherent signal at a given frequency. An on-off modulation of these signals is controlled by trigger signals generatrd by NI model 5782R[2]. The pulse modulation is controlled from a python script that writes the desired waveforms into the memory of each pulse generator. No other modulation was necessary, although replacing the square pulses with other waveforms would have been an option. Signals are attenuated right after generation by 50 dB, to avoid reaching the low power limits of the generators.

The signal generators are all synchronized with a rubidium atom clock that provides a 10-MHz external reference. Without synchronization it is impossible to measure the phase of the signal, because the internal clocks of the different generators naturally drift with respect to each other.

An external magnetic flux is used to tune the frequency of the qubit. The bias flux is generated by voltage biasing superconducting coil with a dc source at room temperature. The coil is placed directly under the sample holder.

[1] Readout from a reflected signal would be possible as well.

[2] In these experiments, the trigger and the digitizer are the same device, which makes their synchronization easier, but is otherwise not necessary.

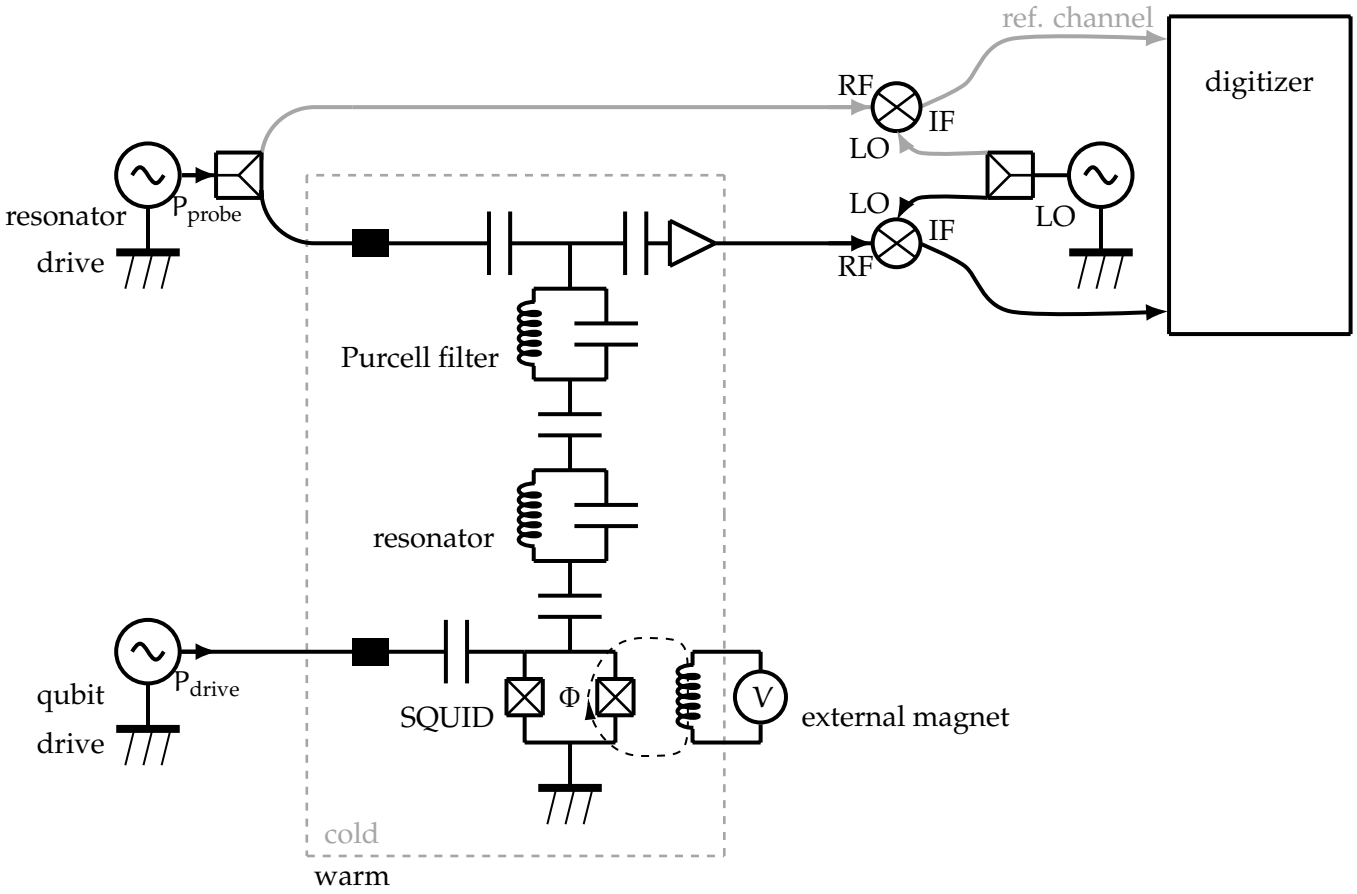

Figure 4.1: **Measurement setup**. Transmission is measured by probing the Purcell-filtered resonator with the input power P_{probe}. The qubit is excited with the power P_{drive}, and the flux of the qubit is tuned with a voltage-biased external magnet. Black boxes denote attenuation, triangles amplification, three-port squares are power splitters and cross-marked circles are frequency mixers.

4.2 Attenuation, amplification, and filtering

The filtering scheme is largely based on that found in Refs. [47] and [36]. As the transmon requires cryogenic temperatures to operate, the sample is placed at the base plate of a Bluefors LD250 cryostat. The sample and the coil are placed in a magnetic shield to prevent eternal fields from disturbing the measurements. The cryostat is cooled down to a base temperature of approximately $10-15$ mK. The cryostat has four plates, roughly at the temperatures 4 K, $600-800$ mK, 50 mK and finally, $10-15$ mK.

The control pulses are filtered and attenuated as they are transmitted in coaxial cables through different temperature stages to reduce noise. The signal powers caused by excitation or de-excitation of the resonator containing a single photon are of the order $\hbar\omega_r\kappa \simeq \hbar \times (2\pi) \times 4.8$ GHz $\times (2\pi) \times 6$ MHz $= 10^{-16}$ W, which is -130 dBm. The noise power associated with thermal noise at room temperatures is of the order $k_B T(f_{max} - f_{min}) \simeq k_B \times 300$ K $\times 1$ GHz $= 10^{-11}$ W, that is, -80 dBm, where the difference of f_{max}

and f_{min} is the bandwidth of the signal. As such, the signal needs to be attenuated at cryogenic temperatures. Thermal noise can leak in from the input coaxial lines carrying the microwave signals, the output coaxial lines carrying the transmitted microwave signal and the dc source for the external magnet. The colder the plate, the smaller the cooling power and so the less thermal noise can be dissipated at that level without warming up the plate. As such, the incoming drive and probe signals are sequentially attenuated inside the cryostat, 20 dB at a time. This attenuation is identical for both lines and adds up to 60 dB for a single line. The cables were measured to attenuate approximately 1 dB per meter, and so should contribute roughly $1-3$ dB. This implies the lines would carry about one photon when probe pulses are generated at a power of slightly below -20 dBm. There are also wide band filters for each input lines at the base plate. They absorb noise to minimize the noise power level.

To prevent noise traveling to the sample from the output side, two circulators are placed in series at the output line, right after the sample. The circulators are three-port components that let a signal pass in one direction from port i to port $i+1$ but reflect about 99% of signals traveling in the opposite direction. The third ports are terminated with $50\,\Omega$. The operating band of the used circulators is $4-8$ GHz. As the circulators may resonate outside this band, a band pass filter, filtering outside $3.4-7.2$ GHz is placed after the circulators. At the 4 K plate, a high-electron mobility transistor (HEMT) provides amplification by 40 dB.

From the base plate to the 4-K plate the flux bias signal was carried on a niobium twisted pair, which is superconducting at these temperatures, to avoid any thermal noise dissipating from a nonzero resistance, and to avoid heat conduction to the base plate.

4.3 Data aqcuisition and digitization

The first step in acquiring the data is to down convert the transmitted signal into frequencies that can be recorded by the digitizer. A microwave signal generator R&S model SGS 100A was used as a local oscillator. At room temperature, the transmitted signal goes through a chain of amplification, attenuation, and band pass filtering. Amplification up to about a millivolt is needed to be able to digitize the signal. Small-value attenuators are used between non-dssipative components to damp parasitic resonances. Band pass filtering is employed to minimize the noise power, i.e. to prevent saturating the amplifiers and the digitizer.

The transmitted signal is then mixed with the local oscillator in a mixer, which down converts the signal to an intermediate frequency $f_{IF} = 70.3125$ MHz. After down conversion, the transmitted signal goes through another cycle of amplification, attenuation and band-pass filtering for the same reasons as discussed above. In order to measure the phase shift caused by the sample and associated with the setup, a reference signal is separated with a power splitter from the probe signal going to the resonator. This sig-

nal goes through a nearly identical cycle of amplification, attenuation, and band pass filtering. Both the transmitted signal and the reference signal are then acquired by the digitizer through different channels.

Depending on the type of measurement, there are two or three types of averaging. In ensemble averaging, N identical pulse sequences are applied in series. The individual data points in a time series are then obtained as the average values over these individual measurements. Depending on the measurement in question, ensemble averaging between 1000 and over a million times was needed. The acquired data is decimated before storage to save space. Before reducing the sampling rate, a moving average over the time series is taken. This kind of boxcar averaging removes signals of shorter timescale than the width of the moving average, but this does not pose a problem assuming the width is chosen small compared with the signal of the highest assumed frequency.

4.4 Measurement schemes

Broadly, all measurements carried out in this thesis are either steady state or pulse modulated. When transmission is measured for much longer than the expected coherence times, it can be assumed that the transmon has reached a steady state. In such *steady-state measurements*, a single data point is obtained as the average over the original time series. All driving pulses are applied simultaneously. Spectroscopy with either one (from the probe) or two (from the probe and drive) microwave tones is carried out as a steady-state measurement. For most of the steady-state experiments, a pulse length of 600 μs was used.

In *pulse-modulated measurements* the delays between the different pulses are important. Drive pulses and transitions between them should be short in comparison with the coherence times of a transmon. That is, shorter than $0.1 - 10$ μs. The digitizer used cannot implement bit flips on consecutive clock periods, which implies that each pulse is separated by at least 16 ns. The resolution of the digitizer also sets a length step of 8 ns for the pulses. The measurement consists of a drive sequence, after which there is a measurement pulse. The lengths of the pulses in the drive sequence is determined by the experiment in question. Pulse lengths between 3 and 10 μs were used for the measurement probes. Pulse-modulated measurement yields a time series, which are integrated over, such that a single time series corresponds to a single data point.

4.5 Parameter estimation

At each value of input frequency f_k and external magnetic flux Φ, transmission responses $\operatorname{abs} S_{21,k}$ and $\arg S_{21,k}$ were measured consecutively N times, with appropriate downtimes. The measured values of the absolute value and the argument of the transmission coefficient were used to construct the real and imaginary parts of the transmission co-

efficient, taken to be the respective mean values. Estimates for peak positions, $\hat{f}_0$, of qubit and resonator–Purcell-filter resonances are obtained via the so-called method of least squares, which amounts to minimizing the sum of the residuals

$$\mathrm{cost}(\boldsymbol{\beta}) = \sum_{k=1}^{M} \left[y(f_k) - \lambda(f_k, \boldsymbol{\beta}) \right]^2 \tag{4.1}$$

where M is the number of input frequency values, $y(f_k)$ are the measured values of either the real, imaginary part or absolute value of the transmission coefficient, and $\lambda(f_k, \boldsymbol{\beta})$ are the values of the distribution model, evaluated at the corresponding input frequencies and parameter values $\boldsymbol{\beta}$. For relatively convex problems, which only have a single global minimum, we employ Matlab's function `fminsearch`. Increasing the number of model parameters usually reduces the convexity. In some cases, a heuristic-based particle swarm optimization algorithm performs better in finding the approximate global minimum. Resulting peak positions, computed at each frequency sweep, i.e. at each value of Φ, were used as input for fitting the transition frequencies (Eqs. 3.18, 3.19 and 3.20) as a function of Φ. As the analytic transition energies contain of the order of ten parameters, the quality of the estimates is improved by gathering data from three data sets, resonances of which correspond to different transitions, and minimizing a global cost, a sum of four costs of the form of Eq. (4.1). The variances of the real and imaginary parts of the transmission coefficient are estimated from the background of the signal. Thus, variances are approximated to be equal at each value of input frequency. Estimated variances are propagated into variances in the peak positions, according to

$$\boldsymbol{\Sigma}(\{\beta\}) = \mathrm{inv}\left(\mathbf{J}^{\mathsf{T}}\mathbf{W}\mathbf{J}\right),$$

where $\boldsymbol{\Sigma}(\{\beta\})$ is the covariance matrix, and the elements of the Jacobian

$$\mathbf{J}_{kl} = \frac{\partial \lambda(f_k, \boldsymbol{\beta})}{\partial \beta_l},$$

are evaluated at the best fit parameters, and the weights are given by the diagonal matrix, with the martix elements

$$\mathbf{W}_{kl} = \sigma[y(f_k)]^{-2}\delta_{kl}.$$

Fit parameter variances are obtained as the diagonal elements of $\boldsymbol{\Sigma}(\{\beta\})$. Resulting peak position variances, $\sigma(\hat{f}_{0,k})^2$, are needed in estimating the variance of parameters such as the Josephson energy, charging energy, and the coupling constants. Monte Carlo sampling is a straight-forward way to obtain confidence limits for the estimates of global parameters. We generate S pseudo-peak-position sets, $\{f_0^*\}_s$, $s \in \{1, ..., S\}$, by perturbing

the estimated peak positions, as

$$f^*_{0,k} = \hat{f}_{0,k} + \sigma(\hat{f}_{0,k}) \times \mathrm{rand}_k,$$

where $\hat{f}_{0,k}$ is the estimated peak position and rand_k is a random number, sampled from a normal distribution with zero mean and unit variance. Here, k ranges over all frequency sweeps of the four data sets. To re-iterate, four sets of peak positions are generated S times. We minimize the global cost, and record the resulting fit parameters S times. Confidence limits for the parameters are given by the ranges $[\beta_{a,\mathrm{min}}, \beta_{a,\mathrm{max}}]$, where 68 percent of fitted β_a are larger than $\beta_{a,\mathrm{min}}$ and smaller than $\beta_{a,\mathrm{max}}$.

Chapter 5

Qubit characterisation results

The sample used in these experiments is fabricated in ETH, Zurich. It is designed by M.Sc. Theo Walter and the staff of the Quantum Device Lab lead by Prof. Andreas Wallraff. The SQUID of the transmon is designed to be symmetric. That is, $E_{J_1} \approx E_{J_2}$ for the two junctions. The qubit is capacitively coupled to two separate transmission line resonators. Both resonators consist of a Purcell filter and an inner resonator, which is capacitively coupled to the qubit. Figure 5.1 shows a Scanning Electron Microscope (SEM) image of the chip. While the upper resonator is connected to ground in all of the experiments, it couples to the qubit, affecting the spectroscopy. From steady-state measurements, we obtain estimates for the most important frequency-independent parameters, which are collected into Table 5.1. From time-domain measurements, we obtain estimates for the coherence times, which are found in Tables 5.2 and 5.3.

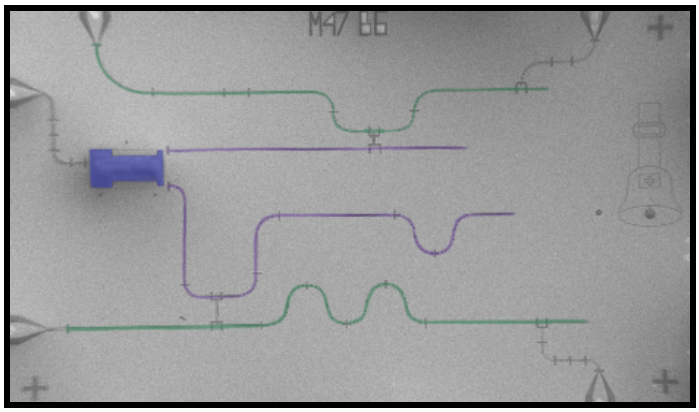

Figure 5.1: **Sample chip under SEM**. The SQUID is within the blue-highlighted region. The inner resonators are highlighted with violet, and the corresponding Purcell filters with green. Original image is grayscale.

Table 5.1: **Frequency-independent parameters**.

Parameter	Estimated value (GHz)	$[CL_{2.5}, CL_{97.5}]$
f_{r_1}	4.80	[4.79, 4.81]
f_{r_2}	8.05	[8.04, 8.07]
$E_{J,max}/(2\pi\hbar)$	23.5	[22.7, 24.3]
$E_C/(2\pi\hbar)$	0.423	[0.412, 0.444]
$g_{q,r_1}/(2\pi)$	0.212	[0.208, 0.216]
$g_{q,r_2}/(2\pi)$	0.491	[0.485, 0.495]

Table 5.2: **Qubit-lifetime parameters** ($f_q = 8.84$ GHz)

Parameter	Estimated value (μs)	$[CL_{2.5}, CL_{97.5}]$
T_1	0.66	[0.60, 0.72]
T_2^*	0.97	[0.785, 1.155]

Table 5.3: **Qubit-lifetime parameters** ($f_q = 5.85$ GHz)

Parameter	Estimated value (μs)	$[CL_{2.5}, CL_{97.5}]$
T_1	4.02	[3.87, 4.17]
T_2^*	0.40	[0.30, 0.50]

5.1 Steady-state measurements

Spurious external fields may act as an additional bias flux, which renders it initially time consuming to find the $g \rightarrow e$ transition of the qubit, which is simply referred to as the qubit resonance. The transmission line resonators, on the other hand, do not change their resonance frequency radically as a function of the flux. Estimating the bare resonator frequency from e.g. the length of the transmission line, the resonator resonance may be measured using one-tone spectroscopy. Maximizing the resonance frequency by tuning the external flux also maximises the qubit resonance frequency, which may be estimated from the plasma oscillation frequency (Eq. (3.5)). Note that the aging of the sample, for example, can cause the plasma oscillation frequency to shift with time. Alternatively, sufficient tuning of the external flux may lead to an avoided crossing with the qubit, which also provides a starting point for the two-tone spectroscopy. This method works with very little preliminary information about the qubit parameters, but is only viable if there occurs an avoided crossing with the resonator. It is possible to design the qubit with a resonance frequency always below the resonance frequency of the resonator, which would

imply the lack of avoided crossing. On the other hand, the flux dependence of the qubit depends on the symmetry of the SQUID. In practice, the SQUID is never exactly symmetric, which means that f_q cannot be tuned arbitrarily low. Instead, the qubit resonance disappears below some frequency. Thus, the avoided crossing may not be observed if the SQUID asymmetry is sufficiently large. As some experiments require avoided crossing between the subsystems, the relative resonance frequencies and the symmetry of the SQUID junctions is often designed to admit them.

Figures 5.2 (a) and (b) show the typical lineshapes of the resonator and qubit resonances. Transmission coefficients are calculated from the measured output voltage amplitude and phase, and from known attenuation and amplification. Inaccuracy in the estimated attenuation leads to an uncertainty of $1-5$ dB. The Purcell filter is observed as a broad peak and the inner resonator as a sharp dip. In experiments where transmission is probed at a single frequency, the frequency was chosen either at the bottom of the dip or near the left peak. Experiments worked in a range of probe frequencies around the resonance, although the chosen frequency affected the frequency and phase of the qubit resonance.

Behavior of the system is best understood in the so-called *linear-response regime*, a regime of sufficiently low input probe- and drive powers, corresponding to a close to zero average number of photons inside the resonator. In this regime the qubit lineshape is Lorentzian, and transitions between higher excited states are negligible. The linear-response regime is not clearly distinct, but may be defined in terms of the observed response, as follows. Assuming P_{probe} is sufficiently low for the linear-response regime, increasing P_{drive} (from asymptotic zero) broadens the qubit resonance. While the lineshape remains Lorentzian, linear-response regime is maintained. Likewise, if P_{drive} is sufficiently in the linear-response regime, increasing P_{probe} ac Stark shifts the peak position. Linear response regime is maintained for negligible shift.

Figure 5.4 (a) shows the transmission coefficient for several values of input drive power, demonstrating the broadening of the resonance. Likewise, Fig. 5.4 (b) shows the response for several input probe powers, featuring the ac Stark shift, (Eq. (3.12)), as well as gradual broadening into a gaussian. Peak positions are estimated from Lorentzian fits (Eq. (3.28)). Standard deviations are estimated from the signal background. Using peak position estimates from the probe power dependence measurement, Fig. 5.4 (c) demonstrates that the qubit peak position is linear in the probe power [36]. Uncertainties for the peak positions are estimated with MC pseudo experiments, using the estimated background variances (see Sec. 4.5 for details). Linear fit yields an estimate $\omega_q/(2\pi) = 8.79$ GHz, for the bare qubit frequency plus the Lamb shift. Approximating the bare frequency plus the Lamb shift as just the bare frequency, and having measured the coupling constant g_{q,r_1}, the average number of photons in the resonator is obtained from Eq. (3.12),

as

$$\overline{n} = -\frac{(\omega_q' - \omega_q)(\omega_q - \omega_r)}{2g_{q,r_1}^2}. \tag{5.1}$$

Setting $\overline{n} = 1$ in Eq. (5.1), we solve for the frequency shift $\omega_q' - \omega_q$, which yields the input probe power $P_{probe}(n = 1) = (\omega_q' - \omega_q)/k \approx -24$ dBm, where k is the slope in the linear fit.

Estimates for the Josephson energy E_J, charging energy E_C, the coupling constants g_{q,r_1} and g_{q,r_2} and the resonator bare resonance frequencies, f_{r_1} and f_{r_2}, can be extracted as fit parameters from flux-dependent qubit spectroscopy. Due to the random jumps in the phase, it was difficult to measure through the entire period of the system as a function of the external flux. Instead, thinner slices of the period are presented in Figs. 5.3 (a), (b), and (c). Figure 5.3 (d) acts as a reference, placing the measured parts within the complete spectroscopy, in terms of the analytic dressed states (Eqs. (3.18), (3.19), and (3.20)). Figure 5.3 (a) shows a two-tone spectroscopy as a function of the drive frequency and the external flux around the avoided crossing with the upper resonator. Figure 5.3 (b) shows the corresponding one-tone spectroscopy as a function of probe frequency and the external flux, for reference. Figure 5.3 (c) also shows a two-tone spectroscopy in the region where the qubit frequency is close to the plasma oscillation frequency. Due to the minimized dependence on the external flux, the qubit is least susceptible to charge dispersion in this region. Consequently, this region is sometimes referred to as the sweet spot. In order to improve the accuracy of the estimates, a global cost, accounting for the data sets of Fig. 5.3 (a), (b), and (c) is minimized (see Sec. 4.5). Parameter uncertainties are estimated from MC pseudo experiments. Results for the estimates are presented in Table 5.1.

5.2 Time-domain measurements

Figures 5.5, 5.6 and 5.7 display the collected data and the corresponding fits. Tables 5.2 and 5.3 collect the estimates and statistical uncertainties obtained from the fits for the π pulse length, qubit lifetime and ensemble-averaged decoherence time (see Sec. 3.2). Short pulse duration in comparison to coherence times leads to shorter qubit and resonator excitation times in comparison to steady state measurements, which thus require higher input powers to excite the qubit. A few dB higher probe power and several dB higher drive power are used compared with the linear-response regime employed in the steady-state measurements. Over a million averages was required to obtain each data point. One data set is measured near the sweet spot, with $f_q \approx 8.841$ GHz. Another data set is recorded at $f_q \approx 5.849$ GHz, which is close to the region

$$\frac{g_{q,r_2}}{f_{r_2} - f_q} = \frac{g_{q,r_1}}{f_{r_1} - f_q}, \tag{5.2}$$

which is satisfied for $f_q = 5.92$ GHz. This region is sometimes referred to as the second sweet spot, because the qubit is in some sense equally far away from each resonator.

Pulse modulation scheme for Rabi experiment is presented in Fig. 5.5 (a), and the resulting Rabi oscillations in Fig. 5.5 (b). Length of the π pulse does not ideally depend on the qubit frequency, but it heavily depends on the drive power. The pulse modulation scheme for measuring the relaxation time T_1 is depicted in Fig. 5.6 (a), and the resulting data and fits are shown in in Fig. 5.6 (b). Both show the expected, exponentially decaying excited state probability. The lifetime of this sample is possibly limited by dielectric losses due to impurities near the junctions. However, the mechanism is not well understood. The pulse modulation scheme for the Ramsey experiment used to measure the ensemble-averaged decoherence time, T_2^*, is presented in Fig. 5.7 (a) and the corresponding data with fits is plotted in Fig. 5.7 (b). Again, data is collected at the two sweet spots. Dephasing times are limited by flux and charge noise. The measured $E_{J,max}/E_C \approx 56$ is still relatively small, which means that the sample is somewhat susceptible to low-frequency charge noise, which is proportional to $\partial E_J/\partial \Phi$ [33]. The effect of the charge noise is thus minimal at the sweet spot. Indeed in this region, decoherence time is nearly limited by the lifetime, whereas at the second sweet spot, where charge dispersion is more noticeable, the decoherence time remains much smaller than T_1.

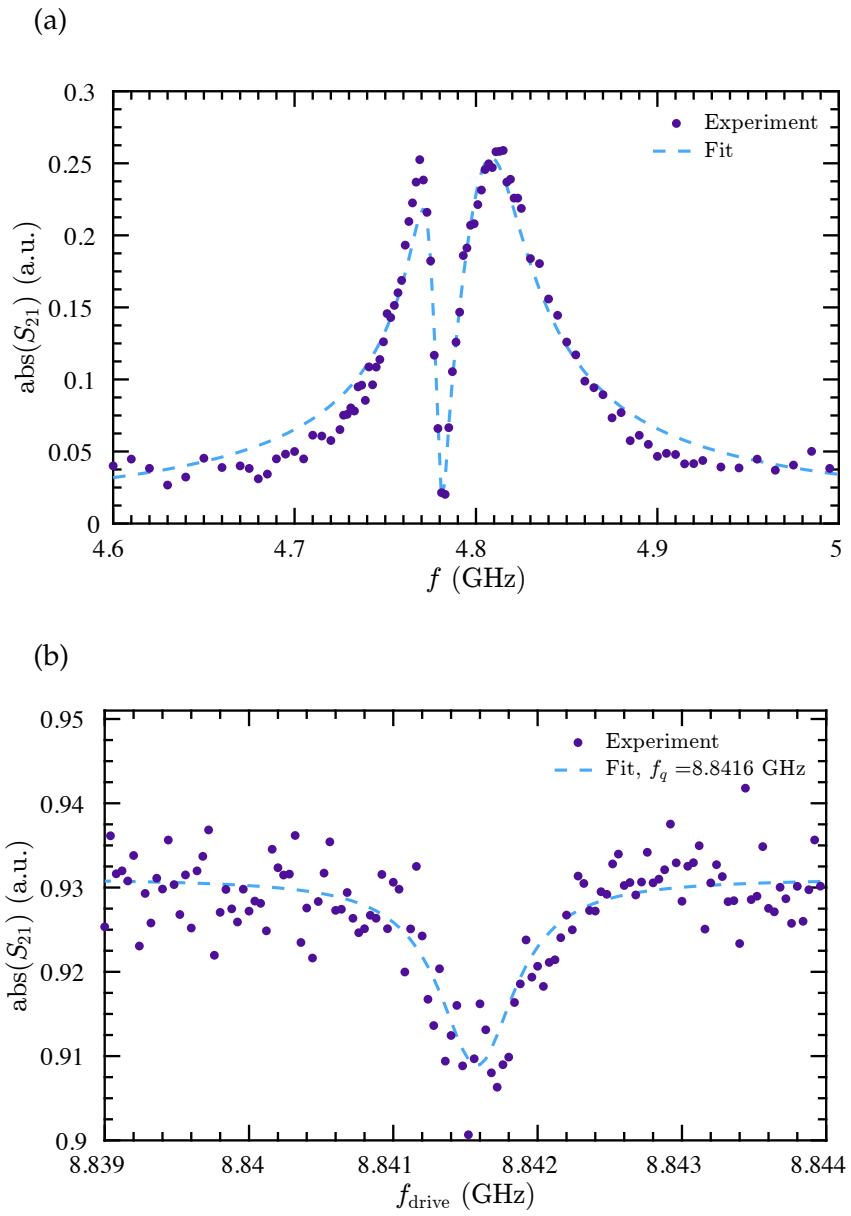

Figure 5.2: **Resonator and qubit lines.** (a) One-tone spectroscopy of the lower resonator (dark blue dots) near its maximum resonance frequency. (b) Two-tone spectroscopy of the qubit at the same external flux, using a probe frequency f = 4.765 GHz. Corresponding Lorentzian fit is denoted with light blue dashed line. The data points in (a) are ensemble averaged over 32 repetitions, while the ones in (b) are averaged over more than 16 000 repetitions.

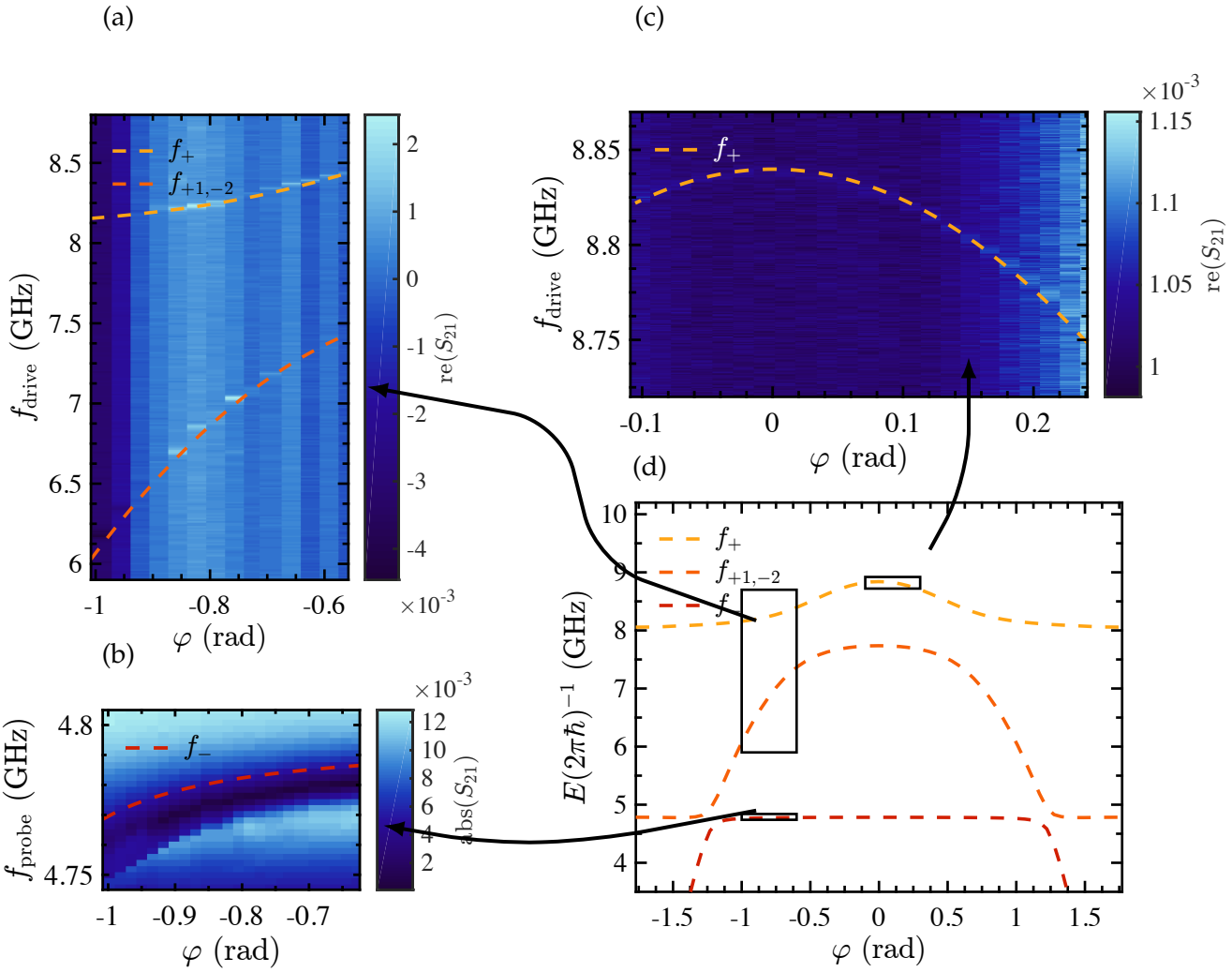

Figure 5.3: **Flux dependent spectrocsopy.** (a), (c) Two-tone spectroscopy of the real part of the transmission coefficient as a function of the dimensionless phase φ and drive frequency (color), with the best fits for the dressed states (dashed lines). (b) One-tone spectroscopy of the absolute value of the transmission coefficient as function of the phase and probe frequency (color) and the best dressed state fit (dashed line). Panels (a) and (b) show the resonances that correspond to the dressed states E_-, $E_{+1,-2}$, and E_+, respectively. Panel (c) shows a closeup of the dressed state E_+ near the sweet spot $f_q \approx 2\pi\omega_p$. See Table 5.1 for a list of parameter estimates obtained from a global fit. (d) Reference figure of the dressed-state-period in the phase.

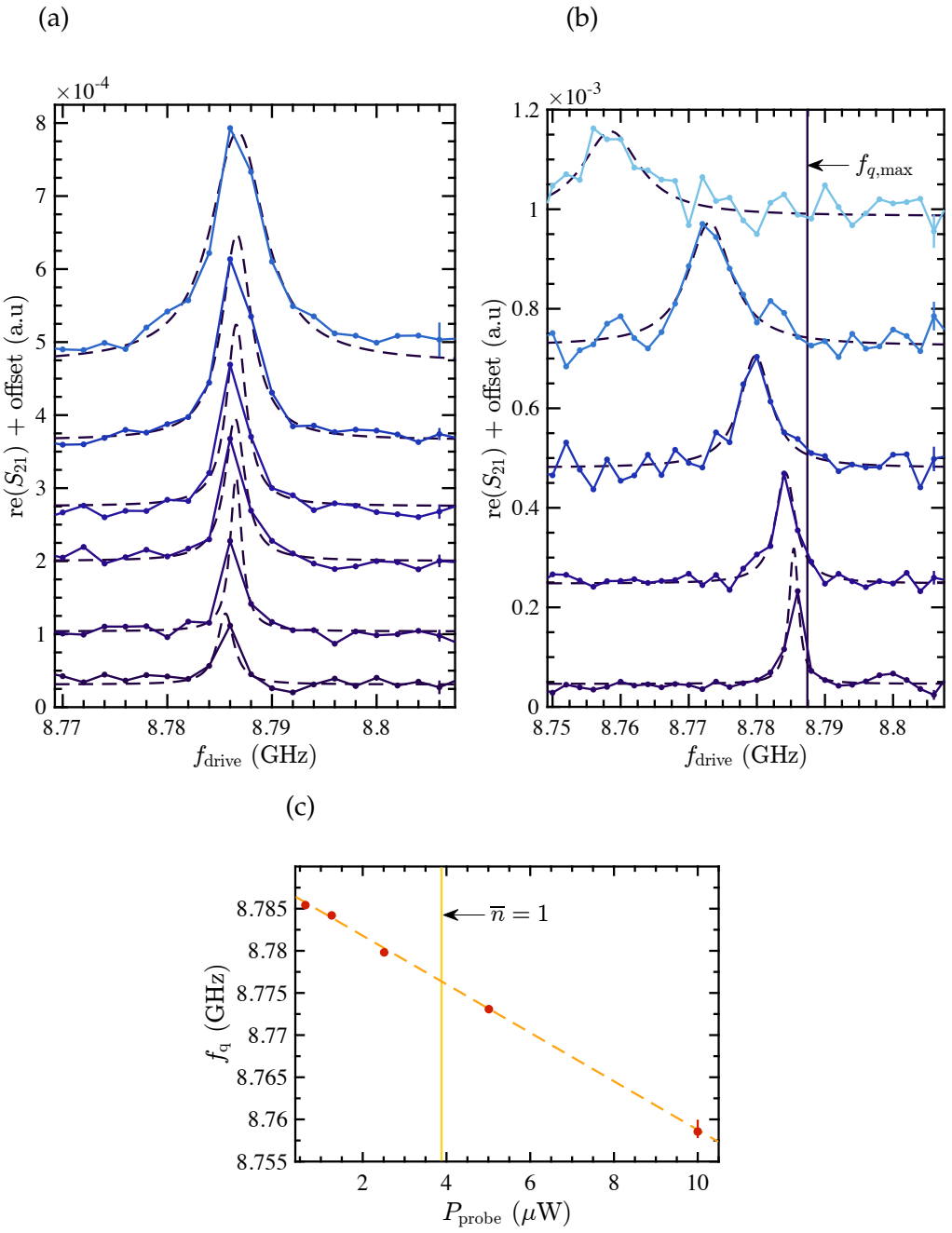

Figure 5.4: **Qubit resonance power dependence.** (a) Transmission coefficient as a function of the input drive frequency, for drive powers $P_{drive} \in [-28\ dBm, -13\ dBm]$ (blue connected points), while the probe power is a constant, $P_{probe} = -19$ dBm. (b) Transmission coefficient as a function of the input drive frequency, for probe powers $P_{probe} \in [-32\ dBm, -20\ dBm]$ (blue connected points). The drive power is kept at a constant $P_{drive} = -24$ dBm. Estimated unshifted qubit resonance $f_{q,max}$ is indicated as a vertical line. In (a) and (b), drive and probe powers are increased in steps of 3 dBm, and ligher curves imply higher input powers. Dark dashed curves show the corresponding Lorentzian fits. Vertical offsets are for clarity. Statistical errors estimated from the signal background for each curve are indicated with a vertical error bar on the rightmost data point. (c) ac Stark shifted qubit resonance frequencies, estimated from (b), as a function of the probe power (red dots), with estimates for statistical errors. Linear fit shown as a dashed line. Estimation for input probe power $P_{probe}(\bar{n} = 1) \approx -24$ dBm is indicated with a vertical line.

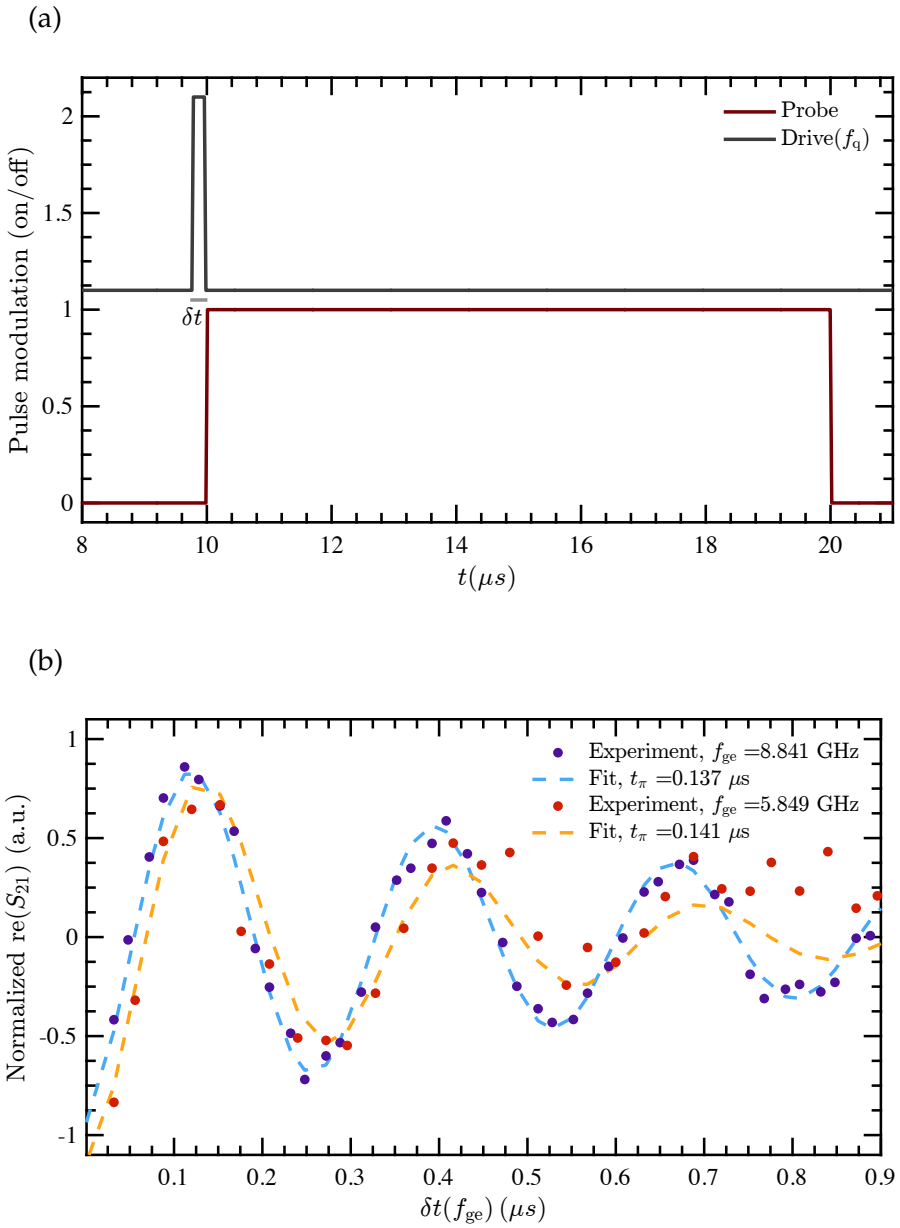

Figure 5.5: **Rabi oscillations.** (a) Pulse modulation scheme. Excitation of varying length of δt is denoted with a gray peak, and the probe pulse with a wide red square pulse. (b) Normalized, integrated transmission coefficients as a function of the excitation time are shown as blue and red data points. Fits to an exponentially damped sinusoidal oscillation are denoted with dashed light blue and orange liness.

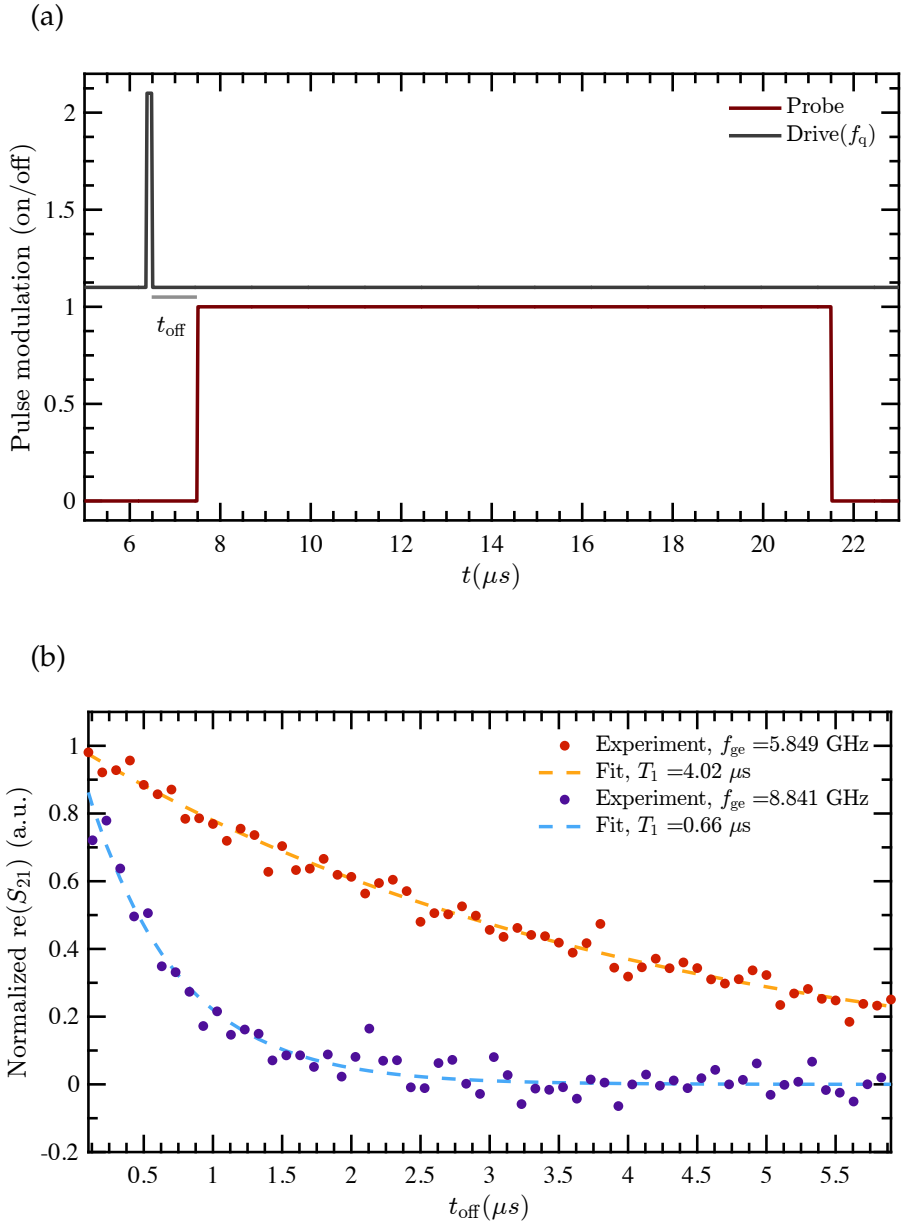

Figure 5.6: **Lifetime measurement.** (a) Pulse modulation scheme. The excitation pulse is denoted with a dark gray peak, and the measurement pulse as a red, wide square pulse. The offset time, t_{offset}, between the excitation and measurement pulse is denoted with a light gray line. (b) Normalized, integrated transmission coefficients as a function of the offset time (blue and red points), with fits to exponential decay (light blue and orange dashed lines).

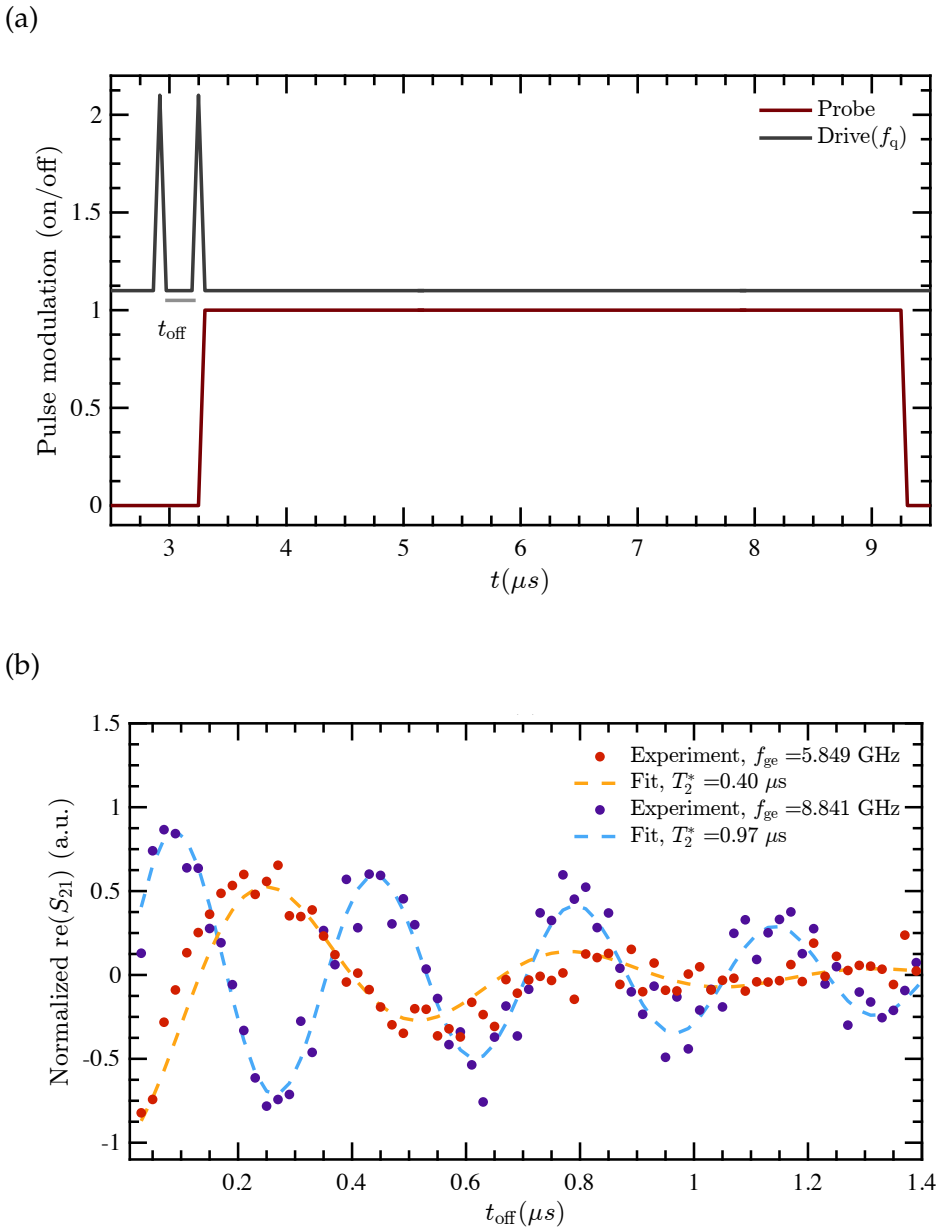

Figure 5.7: **Ramsey fringes.** (a) Pulse modulation scheme. Qubit excitation pulses are denoted with dark gray peaks, and the measurement pulse as a red square pulse. The offset time t_{offset} is denoted as a light gray line. (b) Normalized, integrated transmission coefficients as a function of the offset time (blue and red points), with fits to an exponentially damped sinusoidal functions.

Chapter 6

Conclusions and discussion

We demonstrate a qubit characterization procedure for a transmon-type superconducting qubit, which comprises of a SQUID-loop coupled to two CPW-resonators. We employ a homodyne detection of the transmission coefficient through one of the resonators, and the relevant filtering schemes required for the cryogenic operation of the sample. We also apply drive pulses through a separate line to directly excite the qubit, as well as an external magnet to tune the resonance frequency of the qubit. We measure the most relevant frequency independent parameters, namely the bare resonance frequencies, the Josephson energy, the charging energy, and the qubit-resonator coupling constants, in steady-state spectroscopy, where the probe pulses are long in comparison to the coherence times. Refer to Table 5.1 for the reasults. The spectroscopy is analyzed in terms of analytic dressed states, which approximate the numerically solvable dressed states well. The model could possibly be extended to describe larger systems of qubits and resonators. We estimate statistical uncertainties of the measured parameters with MC pseudo experiments.

We measure the Rabi frequency, lifetime T_1, and ensemble-averaged decoherence time T_2^* in two regions of the parameter space, using drive pulses short or comparable in comparison to the coherence times. Refer to Tables 5.2 and 5.3 for the results. In the region where the qubit frequency is tuned to near maximal frequency, T_2^* is maximized and limited by the lifetime. This is expected, since T_2^* time is limited by flux and charge noise. Sensitivity to charge noise is proportional to $\partial E_J/\partial \Phi$, which is minimized at the maximum of the qubit frequency. For the sample used for the experiments presented in this thesis, $E_{J,max}/E_C \approx 56$, which still allows for some charge dispersion. In the region where the qubit frequency is tuned to approximately equally far from both resonators, the charge dispersion is larger, and as a consequence, T_2^* has decreased. However, the lifetime has increased as the qubit frequency is not close to the resonance frequency of either resonator.

In order to produce arbitrary driving sequences, an arbitrary waveform generator should be used to allow for frequency and phase modulation. The use of parametric amplifier in the place of the HEMT would allow for single-shot measurements that do not

require averaging, implying faster measurements. The ability to infer the qubit state fast is crucial for a practical quantum computer, as the motivation is to improve efficiency. Apart from these suggestions, there are other minor ways to improve the setup, such as employing another set of circulators at the drive line to suppress excitations from decaying through it.

Appendix A

Josephson relations

This section provides a minimalistic introduction and references to the topic of superconductivity. We introduce the phase variable of a superconducting order parameter, the Josephson junction and the relations that describe its dynamics. The difference between two phase variables is used as the coordinate degree of freedom in the Lagrangian formalism. The phase difference will be almost equal to the magnetic flux related to the nonlinear inductance characteristic to the device.

When certain materials are cooled down to low enough, material-dependent, temperatures, a phase transition occurs resulting in a phase with vanishing electrical resistance and other peculiar phenomena. Thus this phase is coined *superconducting* [48]. The phase transition originates from charge carriers forming pairs of two, referred to as *Cooper pairs* [49]. The charge carriers, taken to be electrons for concreteness, repel each other owing to the Coulomb interaction, but also attract nearby positively charged nuclei bound to a lattice. When the thermal energy of the electron is sufficiently low, ions have time to gather around it, shielding its negative charge and attracting another nearby electron. At low temperatures, this configuration may become energetically favourable, effectively pairing up the two electrons. While paired, electrons behave much like bosons[1] Unlike fermions, which obey the Pauli exclusion principle, bosons may all occupy the same quantum mechanical state. Since this state is energetically more favourable the state at which the electron is unpaired, nearly all electrons of the conductor pair up. Although electron scattering off of the ions may transfer energy to and break a Cooper pair, this process is exponentially suppressed at low temperatures. Thus, the electrical resistance, is zero.

In Ginzburg-Landau theory of the superconductivity the superconducting state is de-

[1] Fermions have half-integer spin, while bosons have integer spin. In a bound state, the individual spins add up.

scribed by an order parameter[2]

$$\Psi(\mathbf{r},t) = \sqrt{n(\mathbf{r},t)}e^{i\theta(\mathbf{r},t)} \tag{A.1}$$

where $n(\mathbf{r},t)$ is the Cooper pair density in the superconductor, and $\theta(\mathbf{r},t)$ is a quantum phase variable. The order parameter is sometimes called the macroscopic wave function of the superconductor, and indeed describes a coherent quantum state that satisfies the equation

$$i\hbar\partial_t\Psi(\mathbf{r},t) = \frac{1}{4m}\left[\left(-ih\nabla + 2e\mathbf{A}\right)^2 - 2eA_0\right]\Psi(\mathbf{r},t), \tag{A.2}$$

where A_0 and $\mathbf{A}$ are the scalar and vector potential. This equation coincides with the Ginzburg-Landau equation,

$$\alpha\Psi_r(\mathbf{r}) + \beta|\Psi_r(\mathbf{r})|^2\Psi(\mathbf{r}) + \frac{1}{4m}\left[\left(-ih\nabla + 2e\mathbf{A}\right)^2 - 2eA_0\right]\Psi_r(\mathbf{r}) = 0,$$

which minimizes the Gibbs free energy of the order parameter, when the order parameter is of the form

$$\Psi(\mathbf{r},t) = \Psi_r(\mathbf{r})e^{-i\epsilon t/\hbar} \tag{A.3}$$

for some constant ϵ, and $-2eA_0 = \beta|\Psi(\mathbf{r})|^2$. Here, α and β are functions of thermodynamical critical field and superelectron density in zero field [48], i.e. parameters of specific superconductors. *Josephson junction* is a structure in which two superconducting leads are separated by a non-superconducting barrier. Cooper pairs are able to tunnel through the thin junction. This structure is an essential building block of superconducting qubits. As an electric component, denoted with the symbol of Fig. A.1, the Josephson junction is modelled as a two-port component with four parallel currents [32]: the superconducting current I_S, the displacement current I_D, the normal or quasiparticle current I_N, and the fluctuation current I_F. The normal current $I_N \leqslant VG_N$, where G_N is the normal conductance and V is the voltage across the junction, dominates for large V. The fluctuation current is sourced by thermal, shot, and $1/f$ noises. The displacement current is given by $C\dot{V}$. Dynamics associated with the superconducting current are captured by the two so-called Josephson relations [32],[48]. We follow Ref. [48] to obtain the Josephson relations for an easy special case, which is succinctly presented to connect the relations to the aforementioned formalism and associated variables.

Both superconducting parts of the Josephson junction are described by an order parameter (Eq. (A.1)). Because of the gauge redundancy $\mathbf{A}' = \mathbf{A} + \nabla\chi$, there is also redundancy in Ψ: the phase variable satisfies $\theta' = \theta + 2e\chi/\hbar$. Thus, the gauge invariant phase

[2] A thermodynamical order parameter is any variable that characterises the phase transition. It is zero outside in the symmetrical phase and non-zero in the phase where this symmetry breaks.

Figure A.1: **Symbol for Josephson junction.**

difference across the junction of width $2a$ is given by

$$\varphi := \theta(a) - \theta(-a) + \frac{2e}{\hbar}\big[\chi(a) - \chi(-a)\big], \tag{A.4}$$

where $\pm a$ denotes the boundaries of the barrier. We assume $\mathbf{B} = 0$, such that $\mathbf{A} = \nabla\chi$, which simplifies the calculation, but is generally not needed in order to derive the result. Thus

$$\begin{aligned}\chi(a) - \chi(-a) &= \int_{-a}^{a} d\mathbf{l} \cdot \nabla\chi \\ &= \int_{-a}^{a} d\mathbf{l} \cdot \mathbf{A}.\end{aligned}$$

We find the ac Josephson relation by taking the real part of Eq. (A.2), and simplifying it by assuming an isotropic medium such that $n(\mathbf{r}, t) = n$, a constant. After substituting the square of the supercurrent density, $\mathbf{j}^2$, from

$$\begin{aligned}\mathbf{j} &:= -2e\,\mathrm{re}\left[\Psi^*\big(\frac{\hbar}{m}\nabla - \frac{2e}{m}\mathbf{A}\big)\Psi\right] \\ &= -2e\,n(\mathbf{r}, t)\left[\frac{\hbar}{m}\nabla\theta(\mathbf{r}, t) - \frac{2e}{m}\mathbf{A}(\mathbf{r}, t)\right]\end{aligned} \tag{A.5}$$

into the real part of Eq. (A.2), we are left with the equation

$$-\hbar\dot{\theta} = \frac{m}{2n^2e^2}\mathbf{j}^2 + eA_0,$$

which simplifies the time derivative of (A.4) into

$$\begin{aligned}\dot{\varphi} &= \frac{2e}{\hbar}\int_{-a}^{a} d\mathbf{l} \cdot (\nabla A_0 + \partial_t \mathbf{A}) \\ &= \frac{2e}{\hbar}V,\end{aligned} \tag{A.6}$$

if the current density is continuous at the boundaries: $\mathbf{j}(-a) = \mathbf{j}(a)$. Eq. (A.6) is known as the *phase–voltage relation* or the ac Josephson relation. It states that a constant voltage across the junction introduces a time-evolution for the phase difference. The dc Josephson relation will, in turn, connect the phase difference to the supercurrent across the junction. For this part, we take $\mathbf{A} = 0$ and $A_0 = 0$, and assume the energy ϵ to be time-

independent, which is equivalent to saying that Ψ is of the form of Eq.(A.3). Thus Eq. (A.2) separates into time dependent and -independent parts. Assuming, further, that the effect of the barrier is to provide a constant potential $U > \epsilon$ in the barrier region, and that the current density is nonzero only along the axis parallel to $-a$ to a, denoted by x, the non-trivial part of Eq. (A.2) reduces into the one-dimensional time-independent Schrödinger equation for Ψ_r, namely

$$\frac{\hbar^2}{2m}\nabla^2\Psi_r = (U-\epsilon)\,\Psi_r.$$

Outside the barrier, the solutions are free waves. Inside the barrier, the solution reads [26]

$$\Psi_r(x) = \quad A_1 e^{Kx} + A_2 e^{-Kx} \quad \text{for } |x| < a$$

$K^2 = 2m(U-\epsilon)/\hbar^2$. Let me fix

$$\Psi_r(-a) = \sqrt{n_1}e^{i\phi_1}$$
$$\Psi_r(a) = \sqrt{n_2}e^{i\phi_2}.$$

Demanding that Ψ_r is continuous at $\pm a$, we can solve for A_1 and A_2. Substituting the coefficients into the expression for **j** inside the barrier (Eq. (A.5)), we arrive at

$$j = j_c \sin(\varphi)$$

for a constant j_c, which yields the *current–phase relation*

$$I = I_c \sin(\varphi). \tag{A.7}$$

Appendix B

Quantum phase operator

The phase operator $\hat{\theta}$ is presented as an observable conjugate to the number of quanta, $\hat{n}$, i.e.

$$[\hat{n}, \hat{\theta}] = i. \tag{B.1}$$

This seemingly innocent property can only be satisfied in spaces where n of the basis states $|n\rangle$ either runs from minus infinity to infinity, or is finite [50]. This implies that for a photon field, for example, there is strictly speaking no phase operator. There are, however, various definitions for operators that are functions of a phase, although care must be taken when making assumptions about their properties. Sometimes, such operators are denoted with a wide hat to draw attention to the fact that the phase operator does not necessarily exist independently.

The charge states of the Josephson junction are labeled by how many Cooper pairs have tunnelled through the junction with respect to some reference. As Cooper pairs may tunnel to either direction, the label in these states cane be taken formally to run from minus infinity to infinity. Expanded in this basis, the number operator is given by

$$\hat{n} = \sum_{m=-\infty}^{\infty} m|m\rangle\langle m|.$$

The exponentiated phase operators are expressed in this basis as the bare raising or lowering operators

$$e^{i\hat{\theta}} := \sum_{m=-\infty}^{\infty} |m\rangle\langle m+1|$$
$$e^{-i\hat{\theta}} := \sum_{m=-\infty}^{\infty} |m+1\rangle\langle m|.$$

They are unitary and satisfy the commutation relations

$$[\hat{n}, e^{\pm i\hat{\theta}}] = \pm e^{\pm i\hat{\theta}}.$$

Clearly, the operator $\cos(\hat{\theta})$ can be expanded in the Cooper pair number basis as

$$\begin{aligned}\cos(\hat{\theta}) &= \frac{1}{2}\left(e^{i\hat{\theta}} + e^{-i\hat{\theta}}\right) \\ &= \frac{1}{2}\sum_{m=-\infty}^{\infty}\left(|m\rangle\langle m+1| + |m+1\rangle\langle m|\right).\end{aligned}$$

The eigenstates of the exponentiated phase operator that satisfy $e^{\pm i\hat{\theta}}|\theta\rangle = e^{\pm i\theta}|\theta\rangle$ are given by

$$|\theta\rangle = \sum_{m=-\infty}^{\infty} e^{im\theta}|m\rangle$$

and conversely

$$|n\rangle = \frac{1}{2\pi}\int_0^{2\pi} d\theta e^{-in\theta}|\theta\rangle.$$

The eigenstates are complete in the sense that

$$\frac{1}{2\pi}\int_0^{2\pi} d\theta|\theta\rangle\langle\theta| = \mathbf{1},$$

since

$$\int_0^{2\pi} d\theta e^{i(n\theta - n'\theta')} = 2\pi\delta_{n,n'}.$$

However, the states are not linearly independent or even normalizable, as

$$\begin{aligned}\langle\theta'|\theta\rangle &= \sum_{n=-\infty}^{\infty}\sum_{m=-\infty}^{\infty} e^{in\theta - im\theta'}\langle m|n\rangle \\ &= \sum_{n=-\infty}^{\infty} e^{i(\theta-\theta')n}.\end{aligned}$$

A similar inconvinient feature is encountered e.g. with the eigenstates of the momentum operator, and calls for the concept of Rigged Hilbert spaces [51].

Appendix C

Filtering scheme

Figures C.1 and C.2 represent the attenuation and filtering scheme used inside the cryostat and at room temperature, respectively.

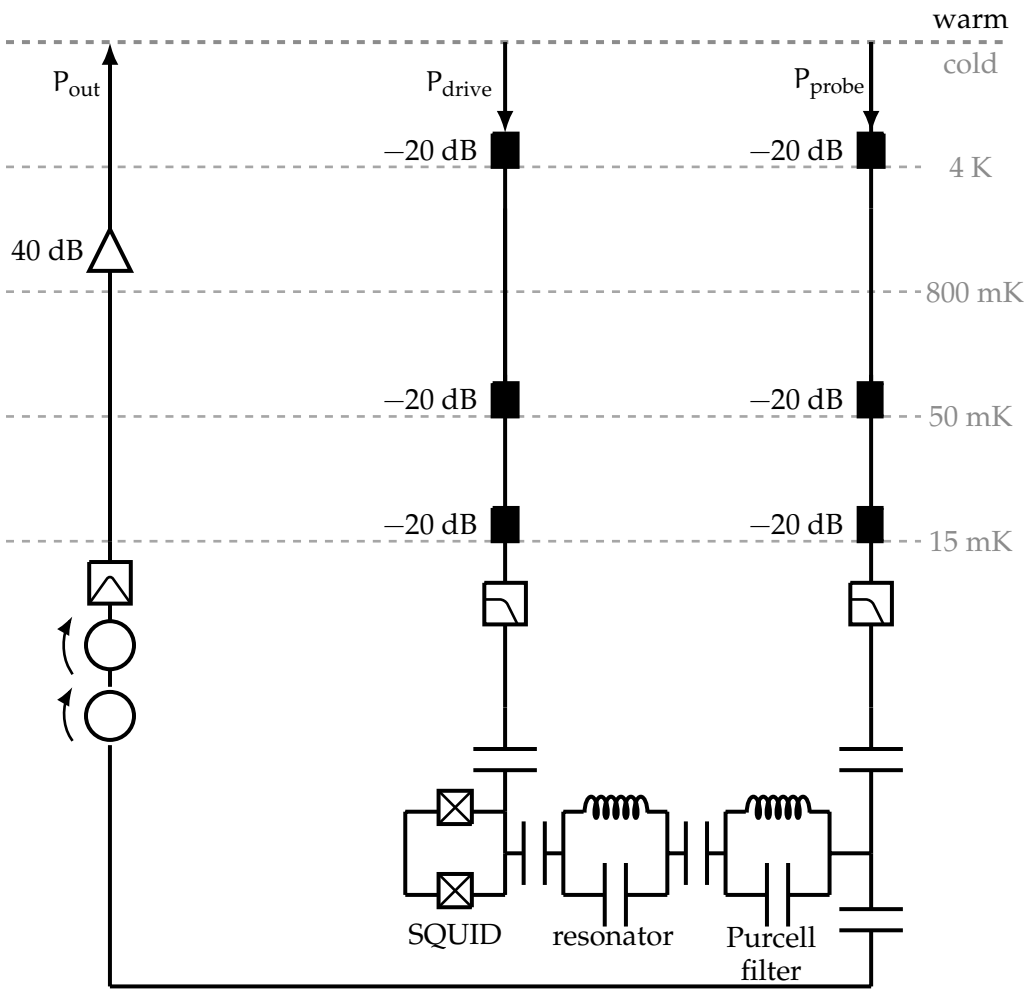

Figure C.1: **Filtering scheme and signal flows inside the cryostat.** Amplifiers and attenuators are denoted with a triangle and a black rectangle, respectively. Circulators are denoted with circles.

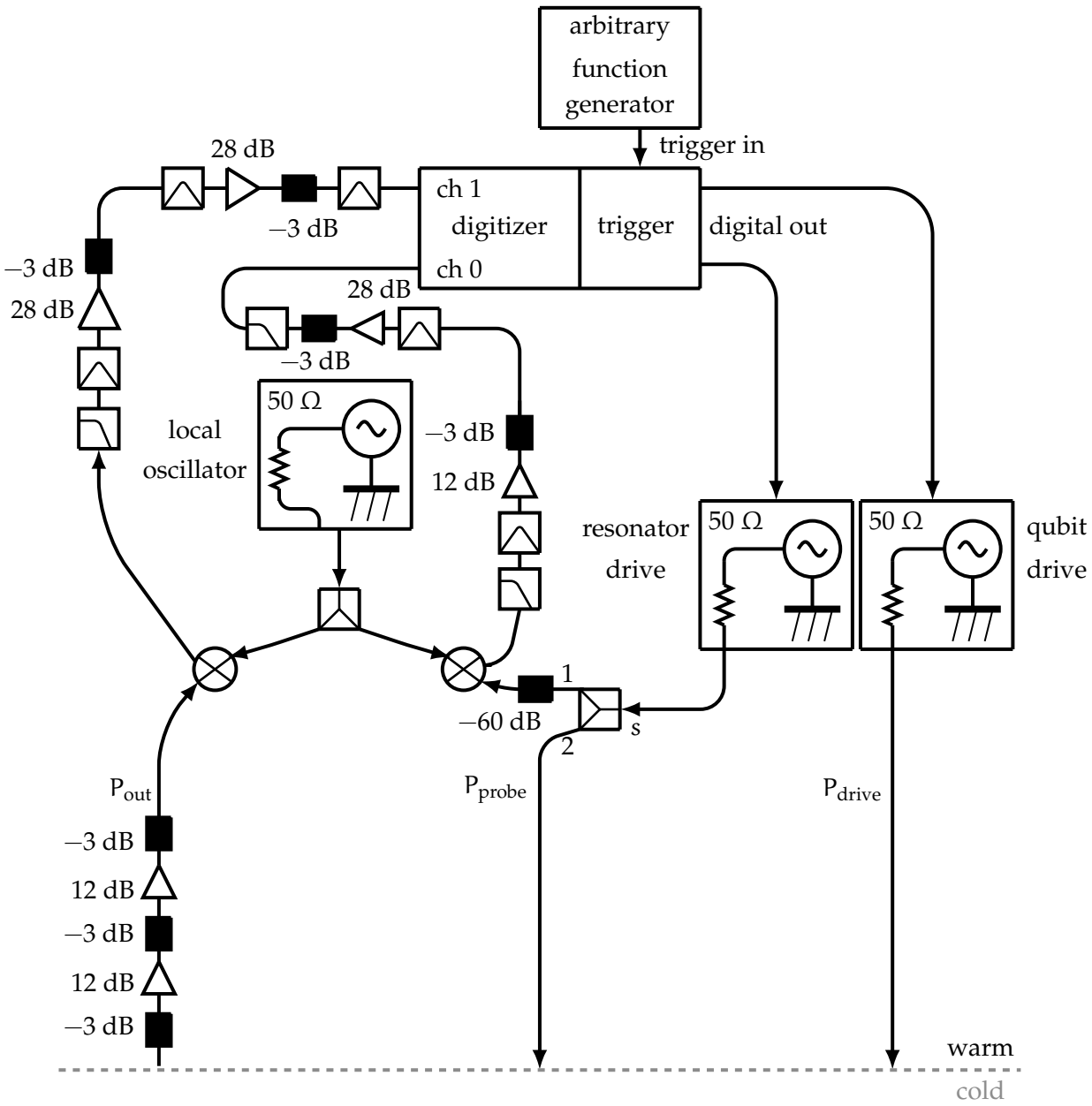

Figure C.2: **Filtering scheme, signal flows and signal processing at room temperature.** Arbitrary function generator, digitizer and trigger are denoted with boxes. Boxes with an ac voltage source ($Z_0 = 50\ \Omega$) denote microwave signal generators. Square boxes with the ports 1, 2 and s denote power splitters, and circular boxes with a cross denote mixers. Low, high, and band-pass filters are denoted with boxes with a decreasing, increasing, or a peaked curve. Amplifiers and attenuators are denoted with a triangle and a black rectangle, respectively. Channel 0 is the reference, and channel 1 the data channel.

Bibliography

[1] D. Deutsch. Quantum theory, the chuch-turing principle and the universal quantum computer. *Proceedings of Royal Society London A*, 400, 1985.

[2] D. DiVincenzo. The physical implementation of quantum computation. *arXiv:quant-ph/0002077*, 2000.

[3] R. Feynman. Simulating physics with computers. *International Journal of Theoretical Physics*, 21, 1982.

[4] V. Denchev *et al.* What is the computational value of finite range tunneling? *Physical Review X*, 6, 2016.

[5] J. Kelly *et al.* State preservation by repetitive error detection in superconducting quantum circuit. *Nature*, 519, 2015.

[6] D. Coppersmith. An approximate fourier transform useful in quantum factoring. *arXiv:quant-ph/0201067*, 2002.

[7] R. Jozsa. Quantum algorithms and the fourier transform. *Proceedings of the Royal Society of London A*, 454, 1998.

[8] L. Grover. Quantum mechanics helps in searching for a needle in a haystack. *Physical Review Letter*, 79, 1997.

[9] N. Shenvi *et al.* Quantum random walk search algorithm. *Physical Review A*, 67, 2008.

[10] I. Georgescu *et al.* Quantum simulation. *Physical Review A*, 67, 2008.

[11] W. Zurek. Decoherence and the transition from quantum to classical – revisited. *Los Alamos Science*, 27, 2002.

[12] A. Steane *et al.* Efficient fault-tolerant quantum computing. *Nature*, 399, 1999.

[13] D. Gottesman. *Stabilizer Codes and Quantum Error Corrections*. Caltech PhD thesis, 1997.

[14] J. Cirac and P. Zoller. Quantum computations with cold trapped ions. *Physical Review A*, 57, 1995.

[15] T. Pellizzari *et al.* Decoherence, continuous observations, and quantum computing: A cavity qed model. *Physical Review Letters*, 27, 1995.

[16] B. Kane. A silicon-based nuclear spin quantum computer. *Nature*, 393, 1998.

[17] D. Loss *et al.* Quantum computation with quantum dots. *Physical Review A*, 57, 1998.

[18] P. Kok *et al.* A scheme for efficient quantum computation with linear optics. *Reviews of Modern Physics*, 79, 2007.

[19] E. Knill *et al.* Quantum computing with photonic qubits. *Nature*, 409, 2001.

[20] C. Nayak *et al.* Non-abelian anyones and topological quantum computation. *Reviews of Modern Physics*, 80, 2008.

[21] A. Córocoles *et al.* Stabilizer codes and quantum error corrections. *Nature Communications*, 6, 2015.

[22] J. Bjorken and S. Drell. *Relativistic Quantum Fields*. McGraw-Hill Book Company, 1965.

[23] B. Yurke and J. Denker. Quantum network theory. *Physical Review A*, 29, 1984.

[24] M. Devoret. *Quantum fluctuations in electrical circuits*. Elsivier, 2001.

[25] U. Vool and M. Devoret. Introduction to quantum electromagnetic circuits. *arXiv:1610.03438*, 2016.

[26] C. Cohen-Tannoudji. *Quantum mechanics, Volume 1*. Wiley, 1991.

[27] H. Goldstein, J. Safko, and C. Poole. *Classical Mechanics (3rd Edition)*. Pearson, 1997.

[28] D. Pozar. *Mcrowave Engineering*. Wiley, 2012.

[29] A. Blais et al. Cavity quantum electrodynamics for superconducting electrical circuits: an architecture for quantum computation. *Physical Review A*, 69, 2004.

[30] M. Devoret *et al*. *Quantum Mechines: Measurement and Control of Engineered Quantum Systems*. Oxford University Press, 2014.

[31] B. Josephson. Possible new effects in superconductive tunnelling. *Physics Letters*, 1, 1962.

[32] K. Likharev. *Dynamics of Josephson Junctions and Circuits*. Gordon and Breach Science Publishers, 1986.

[33] J. Koch. Charge-insensitive qubit design derived from the cooper pair box. *Physical Review A*, 76, 2007.

[34] A. Cottet. *Implementation of a quantum bit in a superconducting circuit*. Paris University PhD Thesis, 2002.

[35] L. Kauffmann and S. Lomonaco. *Mathematics of Quantum Computation and Quantum Technology*. Chapman & Hall/CRC, 1997.

[36] D. Schuster. *Circuit Quantum Electrodynamics*. Yale University PhD thesis, 2006.

[37] C. Gerry and P. Knight. *Introductory Quantum Optics*. Cambridge University Press, 2005.

[38] T. Lindström et al. Circuit qed with a flux qubit strongly coupled to a coplanar transmission line resonator. *arXiv:0704.0727v3*, 2007.

[39] J. Clarke and F. Wilhelm. Superconducting quantum bits. *Nature*, 453, 2008.

[40] M. Nielsen and I. Chuang. *Quantum Computation and Quantum Information*. Cambridge University press, 2010.

[41] S. Patomäki. *Kvanttiajo koherentilla tilalla Jaynesin Cummingsin mallissa*. University of Helsinki, 2015.

[42] D. Schuster *et al.* ac stark shift and dephasing of a superconducting qubit strongly coupled to a cavity field. *Physical Review Letters*, 94, 2005.

[43] A. Abragam. *Principles of Nuclear Magnetism*. Clarendon Press, 1961.

[44] C. Gardiner and P. Zoller. *Quantum Noise*. Springer, 1991.

[45] Personal communications with M.Sc. Theo Walter.

[46] E. Sete *et al.* Quantum theory of a bandpass purcell filter for qubit readout. *Physical Review A*, 92, 2015.

[47] C. Eichler *et al.* Exploring interacting quantum many-body systems by experimentally creating continuous matrix product states in superconducting circuits. *Physical Review X*, 5, 2015.

[48] T. Orlando and K. Delin. *Foundations of Applied Superconductivity*. Addison-Wesley, 1991.

[49] J. Bardeen, N. Cooper, and J. Schrieffer. Theory of superconductivity. *Physical Review*, 108, 1957.

[50] S. Barnett and J. Vaccaro. *The Quantum Phase Operator: A Review*. Taylor & Francis, 2007.

[51] L. Ballentine. *Quantum Mechanics: A Modern Development*. World Scientific Publishing Co., 1998.